

Simulation of transmission electron microscope images of biological specimens

H. RULLGÅRD*, L.-G. ÖFVERSTEDT†, S. MASICH‡,
B. DANEHOLT† & O. ÖKTEM‡

*Department of Mathematics, Stockholm University, Stockholm, Sweden

†Department of Cell and Molecular Biology, Karolinska Institute, Stockholm, Sweden

‡Centre for Industrial and Applied Mathematics, Department of Mathematics, KTH – Royal Institute of Technology, Stockholm, Sweden

Key words. Absorption potential, coherent imaging, computer modelling, contrast transfer function, electrostatic potential, image simulation, inelastic scattering, modulation transfer function, phantom generator, software package, transmission electron microscopy.

Summary

We present a new approach to simulate electron cryo-microscope images of biological specimens. The framework for simulation consists of two parts; the first is a phantom generator that generates a model of a specimen suitable for simulation, the second is a transmission electron microscope simulator. The phantom generator calculates the scattering potential of an atomic structure in aqueous buffer and allows the user to define the distribution of molecules in the simulated image. The simulator includes a well defined electron–specimen interaction model based on the scalar Schrödinger equation, the contrast transfer function for optics, and a noise model that includes shot noise as well as detector noise including detector blurring. To enable optimal performance, the simulation framework also includes a calibration protocol for setting simulation parameters. To test the accuracy of the new framework for simulation, we compare simulated images to experimental images recorded of the Tobacco Mosaic Virus (TMV) in vitreous ice. The simulated and experimental images show good agreement with respect to contrast variations depending on dose and defocus. Furthermore, random fluctuations present in experimental and simulated images exhibit similar statistical

properties. The simulator has been designed to provide a platform for development of new instrumentation and image processing procedures in single particle electron microscopy, two-dimensional crystallography and electron tomography with well documented protocols and an open source code into which new improvements and extensions are easily incorporated.

Introduction

One of the main goals for present-day electron microscopy (EM) is to look at the life processes within a cell at the molecular level. During recent years EM has developed into a most useful tool to study macromolecules, molecular complexes and supramolecular assemblies in three dimensions (3D EM). Three main techniques have been applied: electron crystallography reviewed in Henderson (2004), Glaeser *et al.* (2006), single particle analysis reviewed in Frank (2009) and electron tomography reviewed in Lucic *et al.* (2005), McIntosh *et al.* (2005) and Leis *et al.* (2009). Electron crystallography permits structural analysis of macromolecules at or close to atomic resolution (0.4 nm or better). It relies on the availability of two-dimensional (2D) crystals and has proven especially suited for membrane proteins. Larger biological complexes are preferably studied by single particle analysis, which in favourable cases allows the molecular objects to be examined at medium-resolution (1–2 nm). Notably, this resolution is good enough to permit high-resolution structures of subunits or domains (usually obtained by X-ray crystallography) to be fitted into the large structure at hand. This hybrid approach may reveal the entire complex at close to atomic resolution. Finally, electron tomography

Correspondence to: O. Öktem, Centre for Industrial and Applied Mathematics, Department of Mathematics, KTH – Royal Institute of Technology, SE-100 44 Stockholm, Sweden. e-mail: ozan@kth.se.

Current address: H. Rullgård, Comsol AB, Tegnérgatan 23, SE-111 40 Stockholm, Sweden.

Current address: L.-G. Öfverstedt, Structural Cellular Biology Unit, Okinawa Institute of Science and Technology, 1919-1 Tancha, Onna-son, Kunigami-gun, Okinawa, Japan.

can provide structural information at the molecular level in the context of the cellular environment. Most importantly, small cells or sections through larger cells or tissues can be studied as cryospecimens with a close-to-life preservation as shown by Al-Amoudi *et al.* (2004) and Leis *et al.* (2009). The resolution is presently limited to 4–5 nm but it seems reasonable to reach higher resolution in a near future. The docking approach would then be realistic, which will help identifying and characterizing the molecular complexes observed. It should finally be recalled that electron tomography examines the supramolecular assemblies as individual objects. This is essential as within the cell these complex structures are likely to be dynamic, changing conformation and subunit composition, and interacting, often transiently, with other molecular assemblies and cellular structures. Thus, often in conjunction with other methods such as X-ray crystallography, mass spectrometry and single particle analysis, as shown in Robinson *et al.* (2007), Steven & Baummeister (2008), electron tomography is likely to be a most efficient tool to visualize the supramolecular structures at work, which will help us understanding how they operate within the cell at the molecular level.

Bearing in mind this striking development and the future expected potential of 3D EM, it is anticipated that simulation of electron images will play an increasingly important role in future molecularly oriented EM. A molecular model (phantom), created by means of a phantom generator using information stored in databases, can together with a simulator be used for *in silico* EM imaging. Ideally, background variability and noise are also properly incorporated into the image. Such a tool will be valuable for identifying and characterizing molecular objects in electron images of isolated objects as well as of objects in the cellular environment. Furthermore, a simulator is also necessary to easily and cost-efficiently test and evaluate the impact of new image processing methods as well as novel data collection techniques and improved instrumentation (see further Section 'Usefulness and Significance').

For many years, simulators have been developed to be used in EM studies of biological specimens. Some of the most well-known are contained in software packages for single particle analysis and Electron Tomography (ET) such as Xmipp by Sorzano *et al.* (2004), TOM Toolbox: Acquisition & Analysis for Electron Tomography (TOM) by Nickell *et al.* (2005), System for Processing Image Data from Electron microscopy and Related fields (SPIDER) by Frank & Shimkin (1978), Shaikh *et al.* (2008) and Electron Microscopy Analysis (EMAN) by Tang *et al.* (2007). The simulation functionality is used for evaluation of reconstruction methods for electron tomography in Marabini *et al.* (1997) and single particle in Marabini *et al.* (1998), Sorzano *et al.* (2001). The available functionality includes the possibility to produce a phantom based on information from the RCSB Protein Data Bank (PDB) and to compute Transmission Electron Microscope (TEM) images by

means of projecting the phantom and in some cases adding the effect of the optics and noise. Hence, they can be used to simulate data in a similar manner to the method described in this paper. There are, however, a number of important differences compared to our approach. First, the phantom generators used are too simplistic in the sense that they do not properly account for the physics governing how PDB data is to be translated into a model relevant for TEM simulation. Next, the noise that is added has no clear connection to the physical sources of randomness and is in most cases simply taken as white noise. There is also no calibration protocol for setting values of simulation parameters, neither are the simulators validated. Finally, a number of TEM simulators have also been developed within material sciences. The limited usefulness of these in the context of TEM imaging of biological specimens is discussed in Section 'TEM simulators from material sciences'.

In this study, we present a novel phantom generator and associated TEM simulator and test their validity by comparison of experimental and simulated data from a well-characterized molecular specimen. The aim has been to propose and describe a platform for simulation of TEM imaging of biological specimens that is based as much as possible on physical principles.

Theory and implementation

From a functionality viewpoint, the software components that make up the platform for a TEM simulator can be grouped into two major components:

1. *Phantom generator*: Software allowing the user to generate a synthetic specimen (mathematical phantom) that can be used by the TEM simulator in order to generate a synthetic image.
2. *TEM simulator*: Software allowing the user to simulate TEM imaging of the phantom.

The first approximation we make is to assume that the incident electron and the specimen form a closed system, so any interaction with the environment is neglected. Next, successive incident electrons are independent, so interaction between them is neglected. Furthermore, the incident electron is described quantum mechanically by its wave function while the specimen is assumed to remain in its ground state (stationary state) and therefore modelled classically. Finally, the system is assumed to be stationary where the electron–specimen interaction is modelled by the scalar Schrödinger equation in which the scattering properties of the specimen are fully given by a complex valued function, henceforth called the *scattering potential*.

Phantom generator

A phantom generator essentially needs to allow a user to specify *which* specimen that is to be modelled and then to assemble a *model of the specimen* that can be used in simulating TEM images.

Specifying the specimen. The specification of a biological specimen is made up of the following three parts:

1. *Objects:* This is a specification of a number of molecules (or molecular assemblies), henceforth referred to as *objects*, that will be embedded in the background.
2. *Background:* This is the specification of the background environment encapsulating the objects. It can, e.g. be an aqueous buffer or a carbon foil.
3. *Object distribution:* For each object, one must provide a specification of its 'distribution' in the specimen, i.e. how it is to be distributed in the background environment.

Objects. The phantom generator currently in place assumes that each object is specified by a single file in the PDB format. This file needs to include all molecules (or molecular assemblies) that makes up the object, so for complex objects a user may need to merge several PDB files into a single one.

Background. The phantom generator currently in place can only deal with *in vitro* specimens, hence the background is made up of a slab of aqueous buffer, with flat or curved surfaces. The latter is useful for incorporating influence of uneven specimen thickness which manifests itself as a background gradient in TEM images. The user must therefore provide a definition of these flat or curved surfaces, in which the former is specified by simply providing a thickness. Next, the scattering potential for the background is calculated using an averaging procedure outlined in Appendix B2. Finally, the background always has a natural random variation (granularity) which in single particle analysis is often referred to as 'structural noise'. Modelling the background as a continuum medium might lead to an artificially uniform background which in some situations is not acceptable. We have therefore provided the possibility to include such granularity of the background. The background granularity is generated in two steps as follows. First a small spherical particle with randomly varying potential is generated based on a user provided specification of overall size and contrast. Next, a number of such particles are placed with random positions and orientations in the sample. The number of particles is chosen so that their total volume equals the volume of the sample. The average absolute value of the potential within one such particle, measured in volt, is given for each of the background simulations.

Object distribution. The specimen is made up of a number of objects distributed throughout the background at specific positions and in specific orientations. A user has two ways of describing how objects are distributed.

The first is to let the software randomly distribute the objects. Thus, given a specification of the 'concentration' of each object, the phantom generator will distribute the objects following a uniform probability distribution where the average number of objects per unit volume matches the concentration provided by the user.

The second is to provide an exact specification in a text file of the rigid body motions needed to distribute the objects. The software will read this file and distribute the object accordingly.

Assembling a model of the specimen. A phantom generator needs to create a mathematical model of a specimen relevant for TEM imaging. This is equivalent to generating the scattering potential of the *entire* specimen given a specification of the background, objects, and the distribution of the objects in the background. Besides calculating the scattering potential, this involves difficulties such as how to fuse the scattering potentials of the objects with that of the background and at what resolution (in terms of sampling) to represent the phantom.

Scattering potential of an object. A central part is how to accurately model the electrostatic force field generated by the atoms that makes up the object. For TEM imaging of thin unstained biological specimens, incident electrons primarily scatter against the nuclei of the atoms within the specimen. A model of the electrostatic potential therefore needs to primarily account for this interaction. Empirical evidence suggests that, when properly implemented, the direct approach (explained below) for calculating the potential is accurate enough for simulating electron-specimen interaction occurring in TEM imaging.

In the direct approach, the starting point is to consider the object as a collection of isolated atoms. Then, the electrostatic potential of the object equals the sum of the potentials of the individual atoms. More precisely, consider an object which is a collection of free atoms with nuclei centred at points \mathbf{x}_i . The scattering potential for the entire object is then given as

$$F_{\text{atomic}}(\mathbf{x}) = \sum_i F_i(\mathbf{x} - \mathbf{x}_i), \quad (1)$$

where F_i is the scattering potential for the i th atom. With this approximation, the calculation of the scattering potential of an object is recast to the calculation of the scattering potential of free atoms. The latter is described in detail in Appendix B1.

Note that approaches for electrostatic force field calculations based on solving the Poisson–Boltzmann equation are popular in molecular dynamics calculations, see e.g. Zhang *et al.* (2006) and Bajaj & Goswami (2006). These approaches, which are described in Baker *et al.* (2001), Dolinsky *et al.* (2007) and Chen *et al.* (2007), are designed to accurately model the contributions to the scattering potential from the net charges of the atoms in a molecule and from the ions in the solvent. Using the Poisson–Boltzmann equation to model the electrostatic potential variation within each atom would however require an unrealistically fine sampling of the phantom, so these approaches are not suitable for simulation of TEM images.

Scattering potential of the background. As described in Section ‘Specifying the specimen’, the background is not specified by means of an atomic model. It is rather modelled as a continuum medium. The current software assumes the background is pure water and the potential is calculated from the known concentration of water molecules using an averaging procedure. The precise procedure is described in Appendix B2 and the scattering potential for the background is then set to this average value which may then be adjusted for the granularity.

Even though this procedure assumes that the background is made up of pure water, the approach extends straightforwardly to any aqueous buffer. However, for the type of TEM simulations we consider, we have not found it necessary to provide functionality in the phantom generator for distinguishing between different buffer compositions. We have therefore settled with using pure water as background.

Fusing the background and object potentials. In order not to create artificial contrast, it is important that the object is enclosed by a bounding box large enough that the contribution to the scattering potential from the enclosed object is negligible at the boundary. Our method for calculating the contribution by the object only accounts for the contribution from the nucleus of the atoms that make up the object, see Appendix B for the details. This contribution vanishes a few tenths of a nanometre outside the molecule, so it is rather straightforward to create a bounding box large enough that the contribution to the scattering potential from the object is negligible at its boundary.

TEM simulator

The task of simulating a TEM image can naturally be broken down into simulating the (1) electron–specimen interaction, (2) optical system and (3) detector. Furthermore, one must also account for the blurring caused by the partial incoherence stemming from incoherent illumination and inelastic scattering.

First, the electron is treated quantum mechanically and the specimen classically. Next, we consider a stationary model and assume that the wave function for a single electron can always be written in the form

$$\Psi(\mathbf{x}, t) = u(\mathbf{x}) \exp\left(-i \frac{\hbar k^2}{2m} t\right), \quad (2)$$

where $u: \mathbb{R}^3 \rightarrow \mathbb{R}$ is a function accounting for the spatial variation, m denotes the relativistic mass of the electron, \hbar is the reduced Planck constant, and k is the electron wave number (so $k = 2\pi/\lambda$ where λ is the electron wavelength).

As we only have a stationary model, it is clear that the task of TEM simulation reduces to simulating the spatial variation u as the electron scatters against the specimen and travels through the TEM optics and reaches the detector. For this reason, this

spatial variation u will henceforth be referred to as the *electron wave*.

Electron–specimen interaction. The starting point is to assume that we have perfect coherent imaging, i.e. the incoming electron wave is a monochromatic plane wave (coherent illumination) and electrons only scatter elastically. Once the electron leaves the condenser and until it scatters against the specimen, it is assumed to travel along a straight path parallel to the optical axis of the TEM. Hence, electron wave u_{in} for the incoming electron is of the form

$$u_{\text{in}}(\mathbf{x}) = \exp(i \mathbf{k} \cdot \mathbf{x}), \quad (3)$$

where ω denotes the directional vector of the TEM optical axis (typically one chooses the coordinate axis such that $\omega = (0, 0, 1)$). This incoming electron will henceforth be referred to as the *incident electron*.

For perfect coherent imaging, the scattering potential that fully characterizes the scattering properties of the specimen is given as

$$F(\mathbf{x}) := \frac{2m}{\hbar^2} e V(\mathbf{x}), \quad (4)$$

where $V: \mathbb{R}^3 \rightarrow \mathbb{R}$ is the electrostatic potential and e is the charge of the electron. The electron–specimen interaction is now modelled by the scalar Schrödinger equation which in the stationary setting can be replaced by the Helmholtz equation as shown in Fanelli & Öktem (2008). By resorting to the high energy approximation, it is possible to provide an analytic expression for the solution of the latter in terms of the scattering potential F . It can be shown, see e.g. Fanelli & Öktem (2008) and Glauber (1959), that the wave emerging from the specimen is phase shifted by an amount proportional to the line integral of the electrostatic potential. Writing this mathematically, we have

$$u_{\text{sc}}[F](\mathbf{x}) \approx u_{\text{in}}(\mathbf{x}) \exp\left(\frac{i}{2k} \int_{-\infty}^{\infty} F(\mathbf{x} + t\omega) dt\right), \quad (5)$$

where $u_{\text{sc}}[F]$ is the electron wave for the scattered electron and F is the scattering potential.

To summarize, $u_{\text{sc}}[F](\mathbf{x})$ in (5) models the spatial variation at a point \mathbf{x} of the scattered wave field generated from a single incident electron, travelling along the optical axis, as it scatters against a specimen characterized by its scattering potential F .

Optical system. The optical system of the TEM is modelled as a convolution operator acting on the electron wave, see e.g. Fanelli & Öktem (2008). To simplify the expressions, the magnification of the optics is set to one and the pixel size of the detector is shrunk by the corresponding magnitude. Let u_{sc} denote the electron wave for the electron on a plane immediately below the specimen, so it is given by (5). Also, let u_{det} denote the electron wave in a plane immediately above the detector. Then, following Fanelli & Öktem (2008) and Hawkes

& Kasper (1994),

$$u_{\text{det}}[F](\mathbf{x}) = \mathcal{F}_{\omega^\perp}^{-1}[\text{CTF}_{\text{optics}} \cdot \mathcal{F}_{\omega^\perp}[u_{\text{sc}}[F]]](\mathbf{x}), \quad (6)$$

where $\mathcal{F}_{\omega^\perp}$ denotes the (2D) Fourier transform in the hyperplane ω^\perp orthogonal to the optical axis ω and CTF is the optics Contrast Transfer Function (CTF) that is given as

$$\text{CTF}_{\text{optics}}(\xi) := \chi_{\text{ap}}(|\xi|) \exp\left(i \frac{\Delta z}{2k} |\xi|^2 - i \frac{C_s}{4k^3} |\xi|^4\right). \quad (7)$$

In the above, ξ is a variable in the reciprocal space with unit nm^{-1} . Next, Δz is the defocus ($\Delta z < 0$ for under focus and $\Delta z > 0$ for over focus), C_s the spherical aberration, and χ_{ap} is the aperture function (also called the pupil function). The latter is the characteristic function of the aperture in the focal plane of the primary lens. In our implementation, the aperture is assumed to be expressible by a radial function and it is given as

$$\chi_{\text{ap}}(s) := \begin{cases} 1 & \text{if } s \leq b \\ 0 & \text{if } s > b, \end{cases} \quad (8)$$

where s is the radial distance, $b := kd_{\text{ap}}/f_p$ with f_p denoting the focal length of the primary lens, and d_{ap} is the physical diameter of the aperture in the focal plane of the primary lens

Detector. The detector is modelled as a rectangular area in the detector plane divided into square pixels. The process of detecting the scattered electron wave is divided into several steps, roughly corresponding to the process that takes place in a physical detector. The basic principle of the detector model is a Poisson counting process in which the expected number of electrons at each pixel is proportional to the squared modulus of the wave function. In order to account for detector quantum efficiencies smaller than 1, the actual detector response is modelled as a probability distribution depending on the number of counts (shot noise). Finally, the image is blurred by a detector point spread function (detector blurring). A more detailed explanation follows.

Shot noise. When an electron wave reaches the scintillator it is localized and the collision results in a burst of photons. Hence, a number of such discrete set of interactions occur between the electron and the scintillator during the formation of an image. The points where collisions occur can then be described as a sum of random point masses which are Poisson distributed with the intensity as expected value.

Stated formally, let $\mu[F]$ denote the random measure modelling the above mentioned sum of random point masses. Then, for any sub-region U of the scintillator plane, $\mu[F](U)$ is a Poisson random variable:

$$\mu[F](U) \sim \text{Poisson}\left(\int_U \text{dose}(\mathbf{x}) I[F](\mathbf{x}) d\mathbf{x}\right), \quad (9)$$

where

$$I[F](\mathbf{x}) := |u_{\text{det}}[F](\mathbf{x})|^2 \quad (10)$$

is the intensity at \mathbf{x} generated by a single electron, dose (\mathbf{x}) is the *incoming dose* at \mathbf{x} , and u_{det} is the electron wave in a plane immediately before the detector which in our case is given by (6). The incoming dose at a point \mathbf{x} on the scintillator is defined as the number of electrons per unit area that would reach \mathbf{x} in the absence of a specimen.

Now, for the purpose of numerical computations, the scintillator is discretized into 'pixels' corresponding to the pixels of the detector. If $U_{i,j}$ denotes the (i, j) th detector pixel centred at coordinate $\mathbf{x}_{i,j}$, then the electron count at the (i, j) th pixel is given as a sample of the random variable $\mu[F](U_{i,j})$. Assume furthermore that both the incoming dose and intensity are constant over the (i, j) th pixel. Then,

$$\mu[F](U_{i,j}) \approx C[F](i, j) \quad (11)$$

with

$$C[F](i, j) \sim \text{Poisson}(A_{i,j} \cdot \text{Dose}_{i,j} \cdot I[F](i, j)), \quad (12)$$

where $A_{i,j}$ denotes the area of the (i, j) th pixel, $\text{Dose}_{i,j}$ the incoming dose at the (i, j) th pixel, and

$$I[F](i, j) := I[F](\mathbf{x}_{i,j}). \quad (13)$$

Note that in almost all cases, $\text{Dose}_{i,j}$ is independent of (i, j) .

Finally, the number of counts in different pixels of the subdivision are treated as independent random variables. If the user chooses to leave out simulation of shot noise, then $C[F](i, j)$ is simply taken to be equal to the expected value of the right-hand side of (12). This is unphysical, but can be useful for simulating noise-free data for testing purposes.

Detector response Next, let C_{gain} and C_{DQE} denote the detector gain and detector quantum efficiency, respectively. The detector response $R[F](i, j)$ at (i, j) th pixel $U_{i,j}$ is defined as

$$R[F](i, j) \sim C_{\text{gain}} \cdot \text{InvGauss}(C[F](i, j), C[F](i, j) \cdot (1/C_{\text{DQE}} - 1)), \quad (14)$$

where $\text{InvGauss}(\mu, \sigma)$ denotes an inverse Gaussian (or Wald) random variable with expected value μ and shape parameter σ . Note that when $C_{\text{DQE}} = 1$, the variance is 0, so

$$R[F](i, j) = C_{\text{gain}} \cdot C[F](i, j). \quad (15)$$

The formula for the variance is chosen to obtain a detector model with the right detector quantum efficiency. The choice of the inverse Gaussian distribution is rather arbitrary, but is motivated by the fact that it is rather simple distribution on the positive numbers, whose mean and variance can be any pair of positive real numbers.

Detector blurring. When an electron collides with the scintillator, it generates a burst of photons which are then recorded at pixels in the detector. These photons will however also be detected not only by that pixel, but also to some extent by nearby pixels. This introduces a correlation (blurring) between the initially independent random variables modelling

the shot noise which has the effect of introducing a coarser granularity to the image. Next, there might be further correlations introduced by other elements of the detector, e.g. due to charge bleeding around spots that have relatively high intensities.

A common approach is collectively to model all these correlations phenomenologically by introducing a convolution. Hence, the data recorded at pixel (i, j) , henceforth denoted by $\text{data}[F](i, j)$, is obtained by forming a discrete, 2D convolution of the response $R[F](i, j)$ with a point spread function

$$\text{data}[F](i, j) := \sum_{k,l} R[F](k, l) \text{PSF}_{\text{det}}(\mathbf{x}_{i,j} - \mathbf{x}_{k,l}). \quad (16)$$

The detector point spread function PSF_{det} is defined in terms of its Fourier transform, the modulation transfer function (MTF), which is taken from Zuo (2000)

$$\text{MTF}(\xi) := \frac{a}{1 + \alpha|\xi|^2} + \frac{b}{1 + \beta|\xi|^2} + c. \quad (17)$$

Note that the parameters a, b, c, α and β are all independent of the specimen.

Partial incoherence. The assumption of perfect coherent imaging, which assumes perfect coherent illumination and only elastic scattering, must be relaxed. This is because both inelastic scattering and incoherent illumination introduces partial incoherence.

The partial incoherence that comes from inelastic scattering is accounted for within the coherent framework by introducing an imaginary part to the scattering potential F , called the absorption (optical) potential, and leaving the expression for the scattered electron wave $u_{\text{sc}}[F]$ in (5) unchanged. Hence, the scattering potential that fully characterizes the scattering properties of the specimen is now given as

$$F(\mathbf{x}) := \frac{2m}{\hbar^2} e(V(\mathbf{x}) + iV_{\text{abs}}(\mathbf{x})), \quad (18)$$

where V is the electrostatic potential and $V_{\text{abs}}: \mathbb{R}^3 \rightarrow \mathbb{R}$ is the absorption potential used when one seeks to model the decrease in the flux, due to inelastic scattering, of the non-scattered and elastically scattered electrons.

Perfect coherent imaging requires an illumination system that is fully coherent, i.e. all the emitted electrons have the same energy and the size of the source is infinitely small. In reality the illumination is only partially coherent. When the spatial and temporal coherence is only partial, the transfer function is the product of the optics transfer function $\text{CTF}_{\text{optics}}$ given in (7) multiplied by two exponential envelope functions, the first defining the attenuation of the high spatial frequencies due to partial spatial coherence, and the second defining the attenuation due to partial temporal coherence, see e.g. Hawkes & Kasper (1994). The final transfer function which replaces

$\text{CTF}_{\text{optics}}$ in (6) is then given as follows:

$$\begin{aligned} \text{CTF}(\xi) := & \text{CTF}_{\text{optics}}(\xi) \cdot \exp\left(-\frac{\alpha_c^2}{4} |\xi|^2 \left(\Delta z - \frac{C_s |\xi|^2}{k^2}\right)^2\right) \\ & \exp\left(-\frac{\Delta E^2 C_c^2}{16k^2} |\xi|^4\right), \end{aligned} \quad (19)$$

where $\text{CTF}_{\text{optics}}$ is given by (7), α_c is the aperture angle of the beam furnished by the condenser lens, ΔE the mean energy spread of the electron beam, and

$$C'_c := \frac{(1 + E_{\text{acc}}/E_0)C_c}{E_{\text{acc}}(1 + E_{\text{acc}}/(2E_0))} \quad (20)$$

with C_c denoting the chromatic aberration and E_0 is the rest energy of the electron. It should be noted that there are more accurate models for the propagation of the image through the optical system, see e.g. Ishizuka (1980). The advantage of these more accurate models is in particular significant in cases when one has strongly scattering specimens. Since we are mainly interested in weakly scattering specimens, we have chosen to work with the simpler model given by Eq. (19).

TEM simulators from material sciences. There are a number of quite sophisticated TEM simulators developed for applications in material sciences that are nicely reviewed in Kirkland (2010). The ones that the authors are aware of require that the entire specimen (objects and background) is specified by an atomic model. Furthermore, many also assume that the atoms in the specimen are ordered periodically. For these reasons, TEM simulators from material sciences have limited usefulness for simulating TEM images of biological specimens.

Despite this, some of these simulators have been used for this purpose. In this context it is worth mentioning Yet another MultiSlice (YAMS) by Dinges & Rose (1995), Müller *et al.* (1998) and SimulaTEM by Gómez-Rodríguez *et al.* (2009). Both are based on the multi-slice approach and both do not assume that the specimen is periodic. In theory, they are more accurate than our approach and among the two, YAMS is the most accurate one as it is based on propagating the mutual coherence function, an approach better suited for dealing with partial incoherence as argued for by Rose & Müller (2003). However, when both YAMS as in Sorzano *et al.* (2001) and SimulaTEM as in Gómez-Rodríguez *et al.* (2009) are used to simulate TEM images of biological specimens, inelastic scattering is not included, molecules are simulated in vacuum, and the detector response is ignored. The effects of the background and noise are 'added' afterwards, a procedure that abolishes whatever advantage regarding accuracy that these simulators might have had to offer over using our approach.

In this context it is worth mentioning another advantage of the multi-slice framework that is relevant for simulating TEM images of thick specimens. For such specimens, multiple scattering could be a dominating phenomena. Since our model for the electron-specimen interaction is based on single scattering, it would be unsuitable for simulating TEM images

of such specimens. As demonstrated in Wall (2006) and Müller *et al.* (1998), the multi-slice framework allows for incorporating multiple scattering into the simulations.

Simulating other sources of errors

There are a number of other sources for errors that one would like to simulate. The TEM-simulator provides an end-user interface for simulating random variations in the tilt geometry and random variations in the optics parameters (most notably defocus).

Calibration protocol

Essentially all simulation methods involve nuisance parameters, i.e. parameters whose values are not available beforehand to the desired degree of accuracy. A calibration protocol refers to a method for setting the values of these nuisance parameters, typically by comparing experimental and simulated data pertinent to the imaging study to be performed. Availability of such a protocol is, therefore, important for optimal usage of the TEM simulator.

Some of the nuisance parameters, such as the detector parameters, are calibrated off-line, i.e. their calibration is not dependent on the specific specimen whose TEM images we eventually seek to simulate. The calibration is done by comparing experimental and simulated blank images generated at a given electron dose. The nuisance parameters are adjusted in a specific order until certain characteristics of simulated and experimental data agree. First the detector gain C_{gain} is adjusted so that the average readout values will agree. Next the MTF parameters are adjusted so that the shape of the power spectra will agree. Finally, the detector quantum efficiency C_{DQE} is adjusted so that the variance (estimated from the histogram) of experimental and simulated data will agree.

There are also nuisance parameters that need to be calibrated on-line, i.e. against experimental data related to the specific specimen whose images one seeks to simulate. One such set of parameters are those that enter when the shape of the background region is to be specified. If it is a slab, then we only need to provide the thickness. In many cases the thickness can be set to match an experimentally measured value (see Section 'Sample preparation'). If experimental procedures are not accurate enough or if one prescribes a more complicated shape for the specimen (not just a parallel slab), then the parameters that enter into this description need to be determined by matching the background gradient of experimental and simulated data. Other nuisance parameters are the ones that steer the amount of granularity in the background. These need to be calibrated against experimental data from a specimen containing only background or alternatively data from a specimen with objects and clearly identifiable background regions. The noise characteristics in the background in the experimental image is characterized

by its histogram (mean value and variance) and a power spectrum. The relevant parameters in the simulator are then adjusted to generate a background in the simulated image with similar noise characteristics as the one in the experimental image.

Results

The validation of the TEM simulator and associated phantom generator is based on systematically comparing experimental and simulated images of TMV virions in aqueous buffer. The nuisance parameters are set by the aforementioned calibration procedure. The calibration is done once, after which a number of simulated images are generated and compared to corresponding experimental images under a variety of different imaging settings.

The specimen

Our validation procedure requires a specimen containing single objects embedded in some background. We chose *in vitro* specimens containing isolated TMV virions because the objects (the TMV virions) are structurally well characterized and their appearance in TEM images is well known. It was e.g. recently used in Clare & Orlova (2010) as a test object to assess the quality of cryo-EM images recorded at 300 keV on a CCD camera. Fully assembled, the TMV virion is a rod-shaped plant virus with a diameter of 18 nm and a length of 300 nm consisting of helically arranged protein subunits around the viral RNA strand. There is an inner channel with a diameter of about 4 nm. The high-resolution structure of TMV has been determined by many methods, see e.g. Namba & Stubbs (1986), Clare & Orlova (2010) and the references therein.

In addition, the calibration protocol can by itself be seen as a validation of the simulator for simulating images of the background only, which in this case is vitrified Phosphate Buffered Saline (PBS).

Sample preparation

For the *in vitro* TMV specimens, a stock solution of TMV (70 mg mL^{-1}) was diluted with PBS, pH 7.4, to 1 mg mL^{-1} . A $3 \mu\text{L}$ aliquot was applied to a holey carbon copper grid (Quantifoil Micro Tools GmbH, Jena, Germany), blotted once for 1 s, flash-frozen in liquid ethane using a Vitrobot Mk2 plunger (FEI, Eindhoven, The Netherlands), and transferred in a vitrified state to the TEM by means of cryo-transfer.

The thickness of the imaged area studied in the specimen should ideally match the thickness that we set for the phantom. For the real specimen, the thickness was estimated experimentally after the image acquisition by 'drilling' a hole in the ice with a focused electron beam and acquiring a new image at 45° tilt. Using simple geometry, one can then estimate the value of the thickness which in our case was 50 nm.

Table 1. Table summarizing the specifications for the TEM used to acquire experimental images. Note that the defocus (denoted by Δz in the text) is not listed here as its value is varied during the imaging.

Parameter	Symbol in text	Value	Parameter	Symbol in text	Value
Acceleration voltage	E_{acc}	200 kV	Spherical aberration	C_s	2.0 mm
Mean energy spread	ΔE	0.7 V	Chromatic aberration	C_c	2.0 mm
Objective aperture diameter	d_{ap}	40 μm	Focal length	f_p	2.7 mm
Condenser aperture angle	α_c	0.1 mrad			

Electron microscopy and determination of the intensity profile of an object

TEM images are recorded using a Philips CM 200 FEG transmission electron microscope (FEI, Eindhoven, The Netherlands) equipped with a TVIPS F224 cooled CCD camera (2048 \times 2048 pixels, TVIPS GmbH, Gauting, Germany) having a pixel size of 24 μm . All images are acquired using 66 000 \times magnification and postmagnification was 1.5 \times , resulting in a pixel size at the specimen level of 0.24 nm. Optical specifications of this microscope relevant for the simulator were summarized in Table 1.

In the recorded electron micrographs the TMV virions could be readily recognized. A typical electron micrograph of virions is presented in Fig. 1(a). The rod-like appearance of the virions is apparent as well as the central channel. A segment of one of the virions has been boxed and is shown at higher magnification in the top image in Fig. 1(b). The phase contrast effects can also be discerned, especially the white halo surrounding the rod (an underfocus of 3 μm).

To better characterize the contrast variation in the experimental image of the virion we further studied the boxed region and determined the intensity profile across the virion (bottom image in Fig. 1b). This profile was obtained by projecting the density along the principal axis thereby providing us with an averaged profile of the contrast variation across the virion, see appendix A for further details.

We collected two sets of images: a defocus series and an electron dose series. Each image was scrutinized visually and an intensity profile of the selected segment was generated. Before we present the results in detail, we will discuss how the parameters required for the simulator are determined.

Calibration of nuisance parameters

The objective of the calibration of the simulator is to assign values for the nuisance parameters, which in our case are the detector and background granularity parameters, in order to provide the best possible performance for the simulator. This is especially important within a validation process that involves quantitative comparisons of experimental and simulated data. The principle behind the calibration procedure is to set values for the nuisance parameters so that the simulator generates

blank and background images that match corresponding experimental images under various imaging conditions, see Section 'Calibration Protocol' for more details.

Calibration of detector parameters. The detector parameters occurring in (14) and (17) are calibrated off-line against experimental blank images (i.e. images recorded without any sample) acquired with flat-fielding correction under two different dose settings; 170 e^-/nm^2 (10 e^-/pixel) and 3400 e^-/nm^2 (200 e^-/pixel). The off-line calibration resulted in the following values of the detector parameters: $a = 0.7$, $b = 0.2$, $c = 0.1$, $\alpha = 10$, $\beta = 40$, $C_{\text{gain}} = 81$, and $C_{\text{DQE}} = 0.38$.

The results of the off-line calibration are shown in Figure 2, where simulated blank images and their histograms and power spectra are compared to experimental blank images and their corresponding data. We see from the figure that there is a good match between experimental and simulated images and their respective histograms and power spectra at both low- and high-dose conditions.

Calibration of background granularity. Parameters necessary for generating background granularity are calibrated on-line against experimental images of background-only. These experimental background-only images are obtained as extracts of sub-regions from images of *in vitro* TMV specimens that did not contain any visible structures. Hence, they correspond to images of the buffer of the *in vitro* TMV specimen, which itself is later used for validation. Now, the power spectra of these experimental background-only images as well as the variance of their histograms are compared against those obtained from experimental blank images taken under the same imaging conditions. It turns out that there is a difference in the power spectrum at low frequencies, though the background contribution is much less than the detector noise even at high dose levels. This is clearly illustrated in Fig. 3 which shows the influence of background granularity parameters for imaging under two defocus values, 3 μm (Fig. 3a) and 6 μm (Fig. 3b). In Fig. 3(c), the power spectra of experimental background images taken at these two defocus values is compared to that of a experimental blank image (Fig. 2a). It is clear that there is no significant difference between these power spectra, so for this case the buffer granularity (structural noise) does not have any

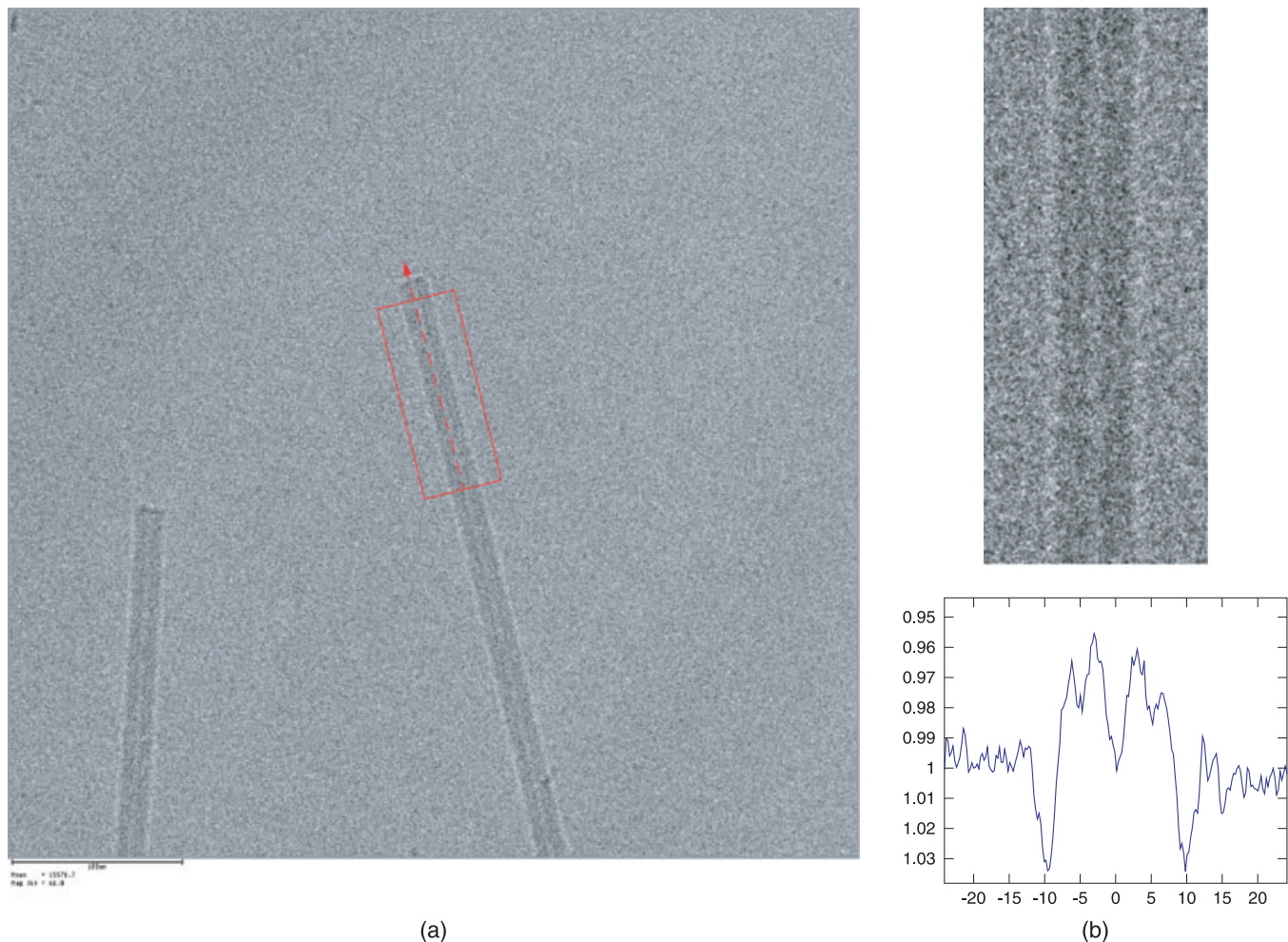


Fig. 1. Calculation of the intensity profile: This particular image of TMV virions is acquired at 3 μm defocus using a dose of about $3500\text{ e}^-/\text{nm}^2$ ($210\text{ e}^-/\text{pixel}$). The region of interest with associated principal axis (dashed arrow) is shown in (a). It is about $120 \times 48\text{ nm}$ (or $500 \times 200\text{ pixel}$) in size and is chosen so that the enclosed portion of the TMV virion is reasonably straight and the background is reasonably homogeneous. In (b) the extracted region of interest is shown aligned, so that the principal axis becomes the vertical axis, and placed 'above' the intensity profile. The intensity profile is obtained by projecting the region of interest along the principal axis.

significant impact compared to stochastic noise from the detector.

Next, to determine at what level the granularity does have an impact on the power spectra, we decided to compare the power spectra of a blank image against that of simulated images of background at different levels of granularity, low, medium and high. This comparison, illustrated in Fig. 3(d)–(f), shows that one has to have a rather high level of granularity in order to see any significant impact on the power spectra. The granularity in the experimental data is somewhere in between medium and high. But even the high granularity level has a low contrast compared to the contrast of molecules (such as the TMVs). The average contrast of the granularity is 0.2 V, so some background granularity might be needed for realistic simulations. Since it will not change the intensity profile of TMV (see Fig. 1 for how the intensity profile is calculated), it

can safely be omitted for the validation. Hence, precise setting of the background granularity parameters is in this case not that important.

The results of the calibration can be summarized as follows: *detector parameters were successfully calibrated off-line against experimental blank images and the issue of optimal on-line calibration of background granularity parameters can safely be ignored for this specific validation.*

Validation of simulator

The objective of the validation is to determine whether the TEM simulator together with the phantom generator and associated calibration protocols are suitable for simulation of TEM imaging of unstained thin biological *in vitro* specimens.

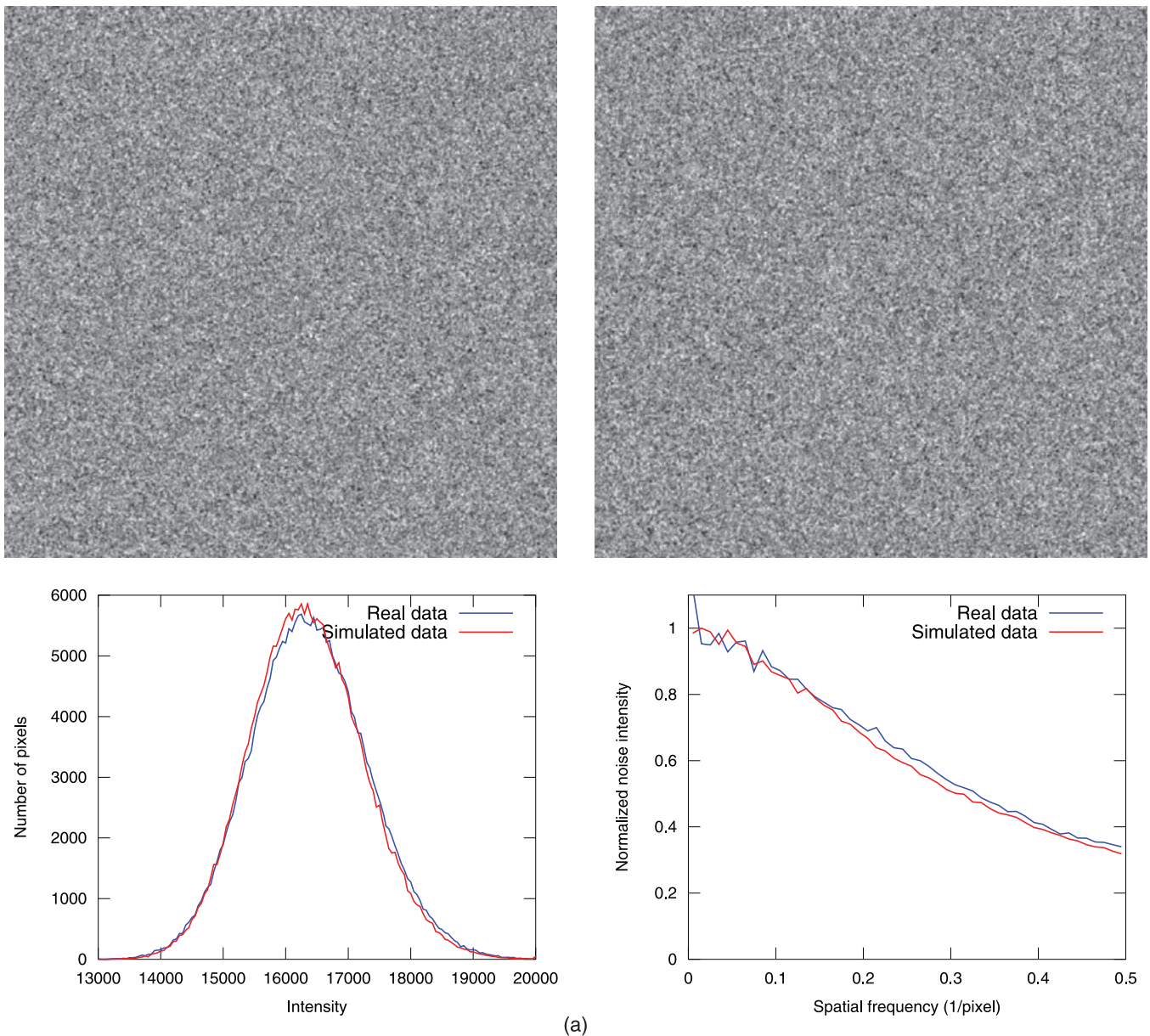


Fig. 2. Off-line calibration of detector parameters against experimental blank images (i.e. images taken without any specimen) against both high- and low-dose data. Results for high-dose, $3400 \text{ e}^-/\text{nm}^2$ ($200 \text{ e}^-/\text{pixel}$), are summarized in (a) where the top row shows experimental (left) and simulated (right) blank images and bottom row shows associated superimposed histograms (left) and power spectra (right). Corresponding results for low-dose, $170 \text{ e}^-/\text{nm}^2$ ($10 \text{ e}^-/\text{pixel}$), are summarized in (b). Note that the horizontal axes for the power spectra plots are in pixels in frequency space, so the highest frequency, which is 0.5, equals the Nyquist frequency.

The simulator with the associated phantom generator was used to generate simulated images of TMV virions to be compared with the experimental images earlier recorded. We first calculated images corresponding both to the earlier recorded defocus and dose series, with no noise added. Subsequently, noise was added to the images to obtain images as similar as possible to the recorded ones.

We were now ready to compare in detail simulated and experimental images of a TMV virion in aqueous buffer, imaged under different defocus and dose conditions.

Variation with underfocus. We examined the TMV virion in focus and at underfocus of $1.5 \mu\text{m}$, $3 \mu\text{m}$, and $6 \mu\text{m}$, and the images recorded in the TEM are presented in the left-hand column in Fig. 4. The corresponding simulated images with

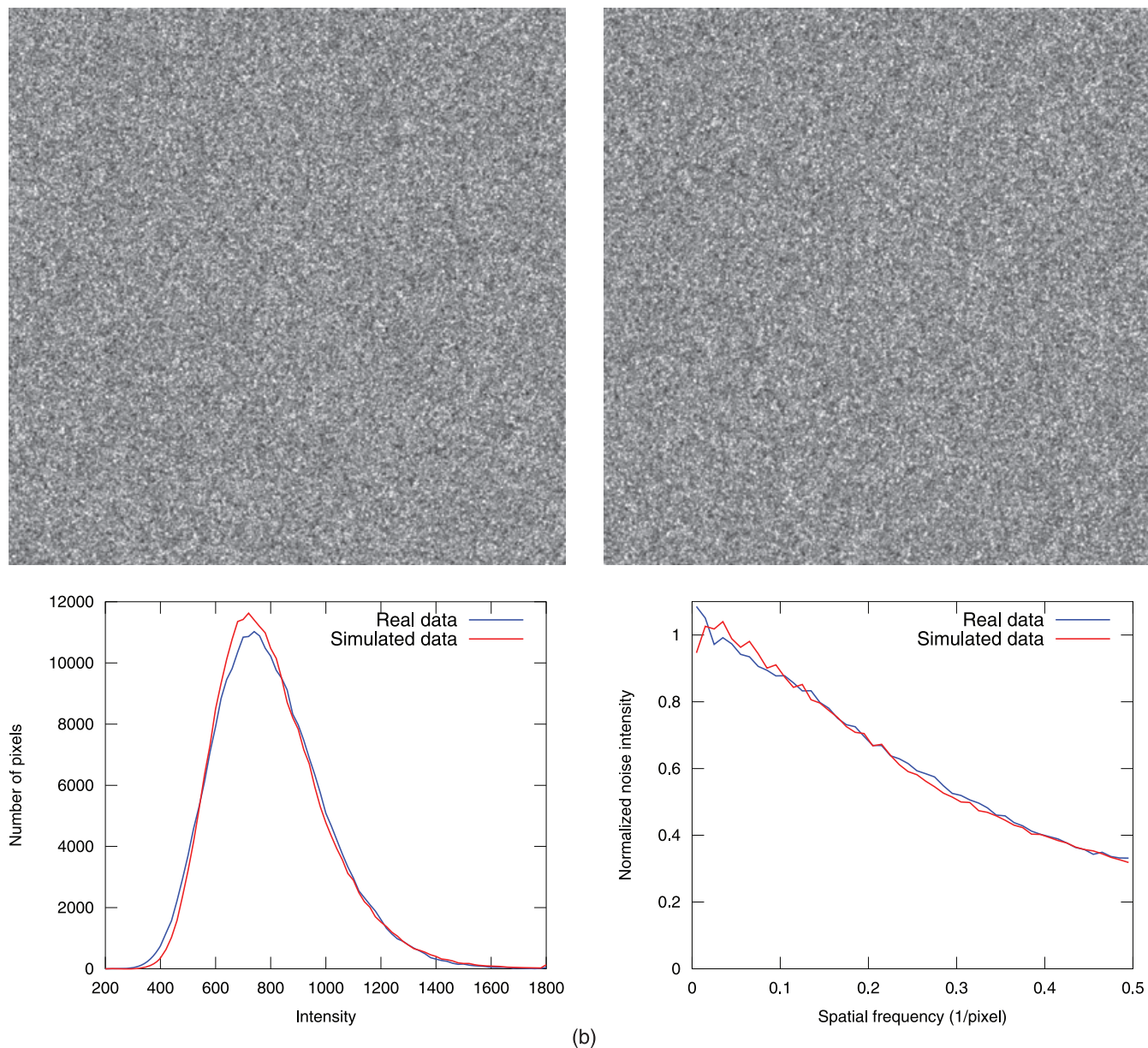


Fig. 2. Continued

no noise are shown in the right column and those including noise in the middle column.

The simulator predicts a series of changes in the image when the degree of underfocus is increased. The gradual alteration of the image is best seen when no noise is present (right-hand column of images in Fig. 4). In focus, the virion is well demarcated, the closely and regularly spaced transverse striations that stem from the helical symmetry of the virion are clearly seen, and the central channel can be discerned. When defocus is increased, various phase contrast effects appear. A thin white rim is seen at 1.5 μm underfocus, and it broadens at 3 μm and even more at 6 μm . In parallel, the diameter of

the image of the virion increases. The transverse striations are clearly seen at both 1.5 and 3 μm underfocus but only weakly at 6 μm , where they have more or less merged into two dark broad bands passing along the longitudinal axis of the virion. The central channel can be discerned in focus but is more clearly seen at higher underfocus and is particularly bright at 6 μm underfocus. A complex interference pattern is evident in the channel at 1.5 μm underfocus but also to some extent at 3 μm underfocus.

When noise is added to the simulated images of the TMV virion, the predicted modifications of the in-focus image in underfocus images are more or less obscured and even hidden

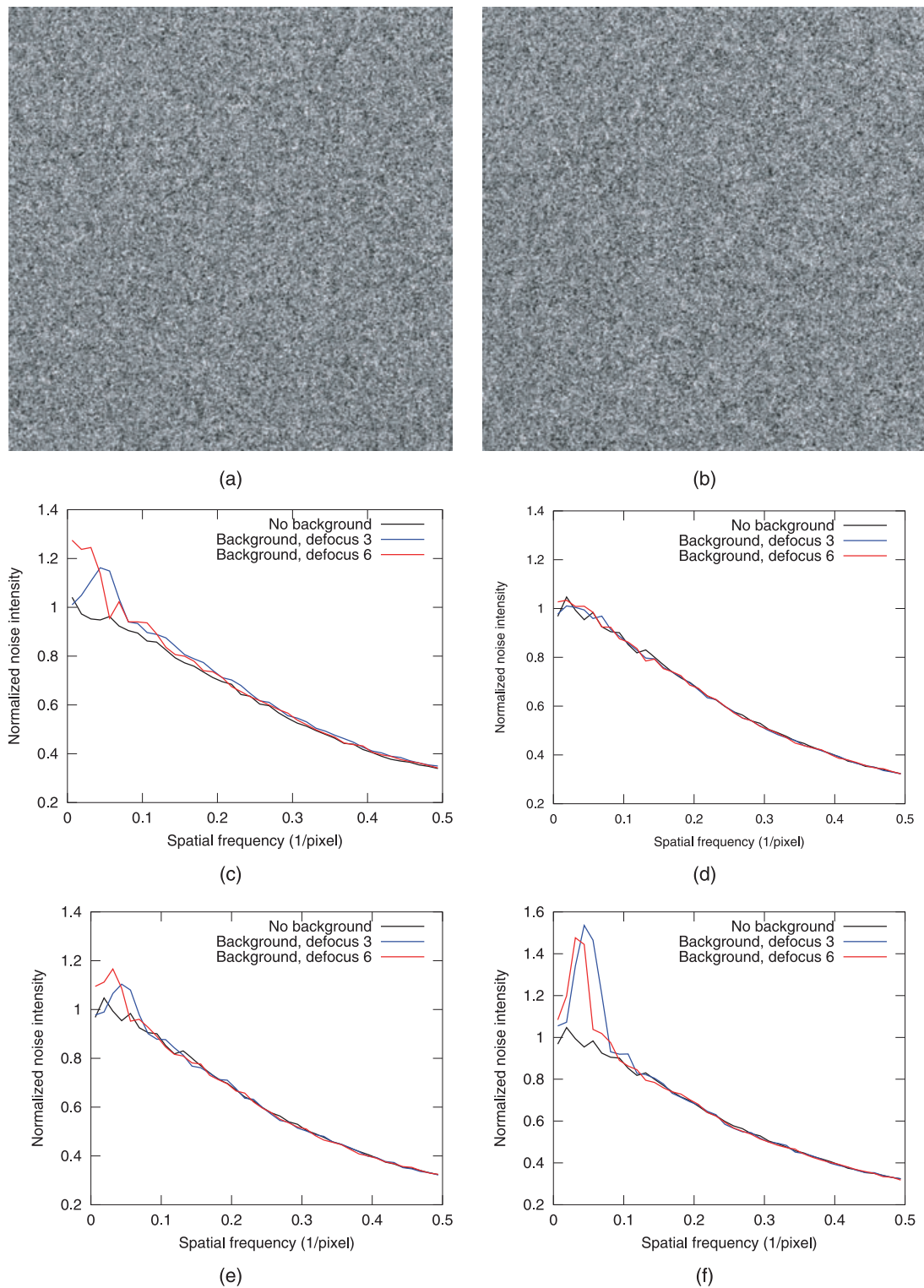


Fig. 3. Influence of background granularity parameters at two defocus values. Panels (a) and (b) show experimental images of the background acquired with a dose of $3300 \text{ e}^-/\text{nm}^2$ ($190 \text{ e}^-/\text{pixel}$) at 3 and 6 μm defocus, respectively. A superimposition of their power spectra together with the power spectra of the top left image in Fig. 2(a) is shown in (c). Finally, (d)–(f) is a comparison of power spectra of a blank image (the top left one in Fig. 2a) against simulated images of background at different levels of granularity. The latter is regulated by the background granularity contrast which is set to 0.05 V (low granularity) in (d), 0.1 V (medium granularity) in (e), and 0.2 V (high granularity) in (f) in more or less arbitrary units. The granularity in the experimental data is somewhere in the range between the medium and high.

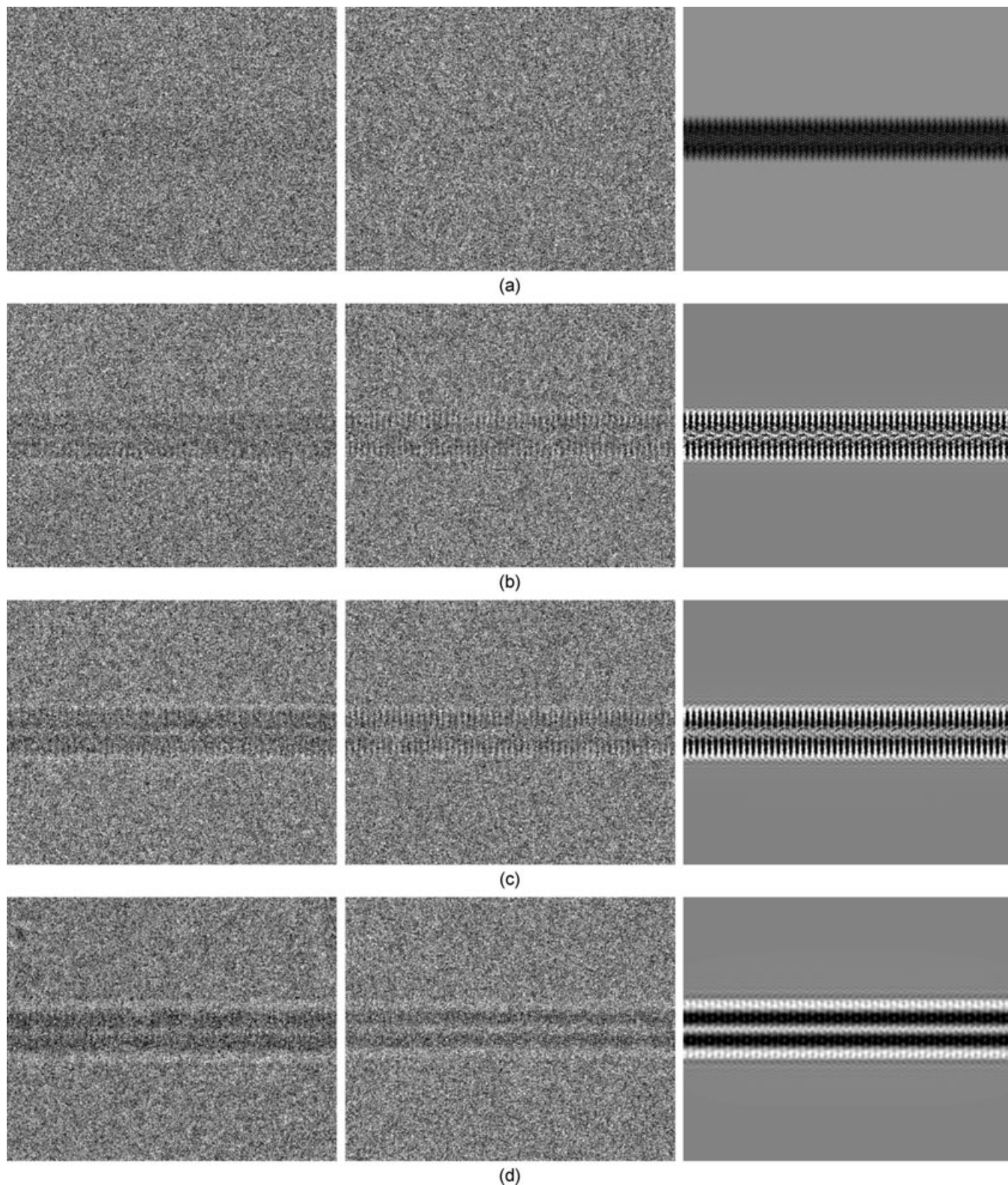


Fig. 4. TMV defocus series: Each row shows experimental (left), simulated (middle), and noise-free simulated (right) images of a portion of a TMV virion acquired at a fixed defocus using $66000\times$ magnification and a dose of $3000\text{--}3500\text{ e}^-/\text{nm}^2$ ($180\text{--}210\text{ e}^-/\text{pixel}$) for experimental images and $3300\text{ e}^-/\text{nm}^2$ ($190\text{ e}^-/\text{pixel}$) for simulated images. The defocus values used for the rows are as follows: $\Delta z = 0\text{ }\mu\text{m}$ in (a), $\Delta z = 1.5\text{ }\mu\text{m}$ in (b), $\Delta z = 3\text{ }\mu\text{m}$ in (c) and $\Delta z = 6\text{ }\mu\text{m}$ in (d). The corresponding intensity profiles are shown in Fig. 5.

(middle column of images in Fig. 4). The virion is not seen at all in focus due to the lack of amplitude contrast, while it is readily recognized at underfocus due to the phase contrast. The transverse striations are discerned at 1.5 and 3 μm underfocus as well as the two longitudinal bands at 6 μm . The white fringes and the central channel are readily seen, while the complex interference pattern in the channel is concealed.

The recorded TEM images of the TMV virion are displayed in the left-hand column in Fig. 4 and should be compared with the simulated ones (with noise) in the middle column. The virion can be vaguely seen in the in-focus image while it is not seen in the simulated image with noise. The most likely explanation for the slight discrepancy is probably that the experimental image has been recorded close to, but not in proper focus. The white fringes and the central channel are similar in the recorded and simulated images. Transverse striations with the expected density and periodicity can be discerned in the experimental images at 3 μm underfocus, but not clearly at 1.5 and 6 μm underfocus. Denser longitudinal bands are also observed in the recorded images at 6 μm underfocus. We conclude that the recorded electron microscopic images are strikingly similar to the simulated ones with noise; the repeated structure and the central channel of the virion are seen as well as the major predicted artefacts due to interference. The main difference is that the recorded images are somewhat more blurred.

To compare recorded and simulated images in a more objective manner, we have determined the density distribution of cross-sections in selected segments of the virion (demarcation of a segment, see Fig. 1). The results for the entire defocus series are presented in Fig. 5; the intensity profiles of the recorded images are compared with the profiles of the corresponding simulated noise-free images (left-hand column in Fig. 5), and the intensity profiles of the simulated images with noise are compared to profiles of the noise-free simulated images (right-hand column in Fig. 5). The recorded image in focus (or close to) shows a vague increase in density, but the conspicuous noise precludes further analysis of the internal structure; in the simulated image no density can be detected. At the various levels of underfocus the same type of basic density profile is seen in recorded and simulated images. The intensity profile of the cross-section of the virion is characterized by two dense peaks separated by a less dense region, the central channel of the virion. In general, as shown in Fig. 5, the intensity profiles of the recorded images are strikingly similar to those of the noise-free as well as the noise-containing simulated images (left- and right-hand columns, respectively). The high degree of similarity is evident when details of the profiles are scrutinised. For example the dense peaks are clearly split at 1.5 μm underfocus. This split is less clearly seen at 3 μm and has vanished at 6 μm underfocus. We conclude that the intensity profiles (and the relative densities) of the cross-sections of the virion change through the defocus series in a similar manner in the recorded and simulated

images. It should also be noted that in the recorded as well as in the simulated images the variance of the background is gradually diminished from the in-focus images to the images obtained at 6 μm underfocus.

To sum up, we recorded conspicuous changes of the density pattern in experimental electron microscopic images of the TMV virion when the focus level was changed from in-focus to an underfocus of 1.5 μm , 3 μm and 6 μm . These changes were examined visually and further verified by determinations of the intensity profiles of cross-sections in selected segments of the virion. The observed changes in the images, including the appearance of artefacts, also appeared in the images generated by the simulator. We conclude that the simulator can provide a series of electron microscopic-like images, outlining the effects of the phase contrast imaging process in underfocus.

Variation with electron dose. It is well established that the electron dose is critical in the analysis of a molecular object embedded in vitrified ice. Revelation of pertinent structural features will require a certain dose, but this dose has to be minimal to avoid, or at least minimize, deterioration of the structure. To test whether the simulator could be useful to predict the properties of an electron micrograph at a certain dose, we recorded a series of electron micrographs of the TMV virion increasing the dose stepwise (exposure for 0.2, 0.5, 1.5 and 3.0 s at a given electron intensity and at underfocus of 3 μm). Simulated images were generated with and without noise and the experimental and simulated images were compared just as done in the analysis of the defocus series of images. The TEM images are presented in Fig. 6, the experimental images in the left-hand column and the simulated ones in the middle (with noise) and the right-hand column (with no noise). Intensity profiles of cross-sections of the various images are displayed in Fig. 7; the profiles of the recorded images are compared with the simulated ones with no noise (left-hand column), and the profiles of the simulated with noise are related to those of the simulated with no noise (right column).

The predicted image of the TMV virion at 3 μm is presented to the right in Fig. 6, and the features of the underfocus image have been described above. In the simulated images with noise added, the characteristics of the virion image becomes gradually more and more distinct as the dose increases. At 3 sec the virion is clearly demarcated by the white rims, the transverse striations are clearly seen, and the central channel is clearly demarcated. We see a similar gradual change in the image of the virion in the recorded electron micrographs (left in Fig. 6), although these are somewhat more affected by noise and the specific features are less evident. For example, the transverse striations are seen after 3.0 s in the recorded image while they are discerned in the simulated image after 1.5 s. The intensity profiles presented in Fig. 7 provide additional information. It can be clearly seen how the signal to noise ratio affects the image. The intensity fluctuations after 0.2 s

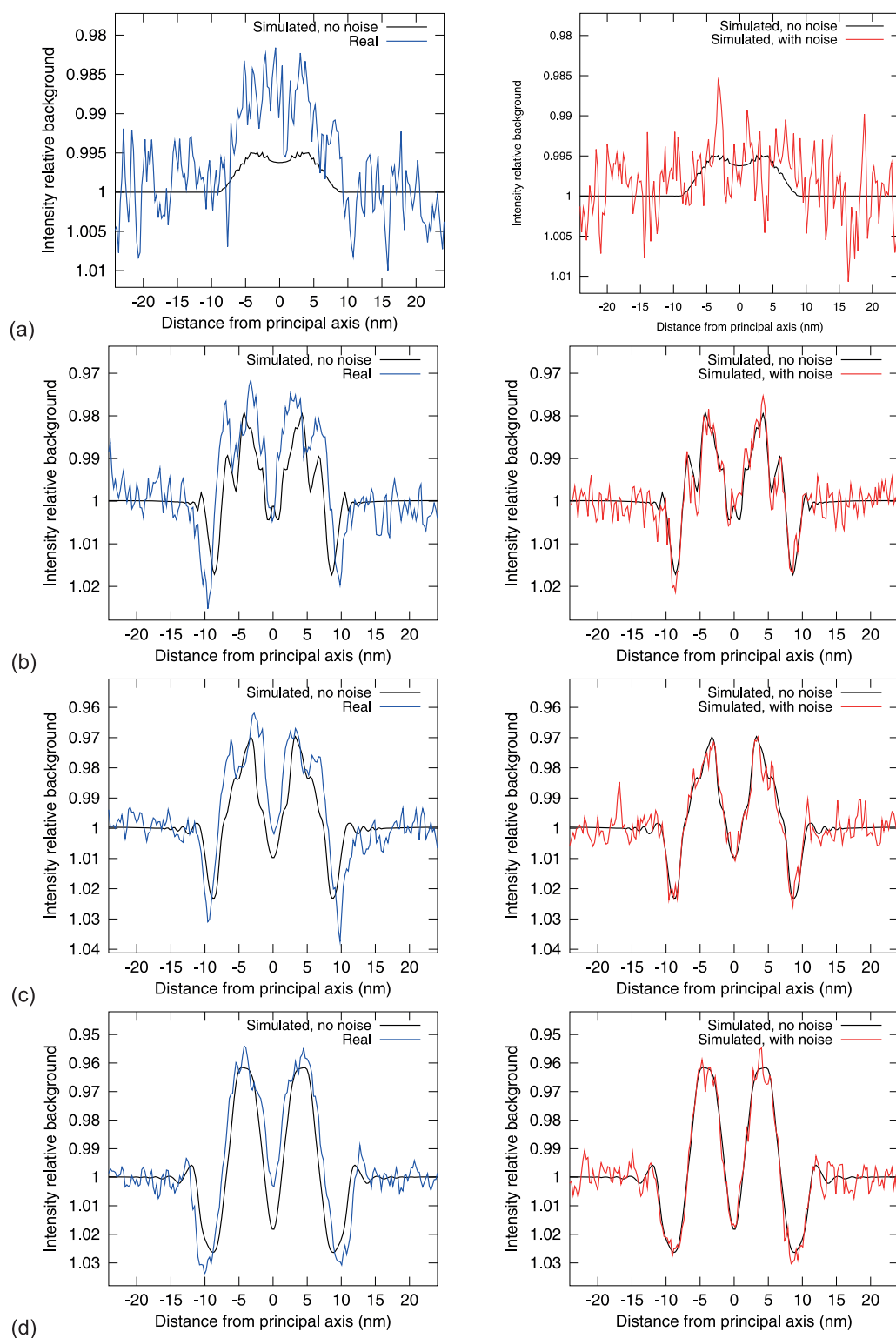


Fig. 5. Intensity profiles in a defocus series: Each row compares intensity profiles of images of a TMV virion recorded using a fixed defocus. The right figure compares profiles from noisy and noise-free simulated images and the left figure compares profiles from experimental and noise-free simulated images. The defocus values used for the rows are as follows: $\Delta z = 0 \mu\text{m}$ in (a), $\Delta z = 1.5 \mu\text{m}$ in (b), $\Delta z = 3 \mu\text{m}$ in (c) and $\Delta z = 6 \mu\text{m}$ in (d). The images are shown in Fig. 4.

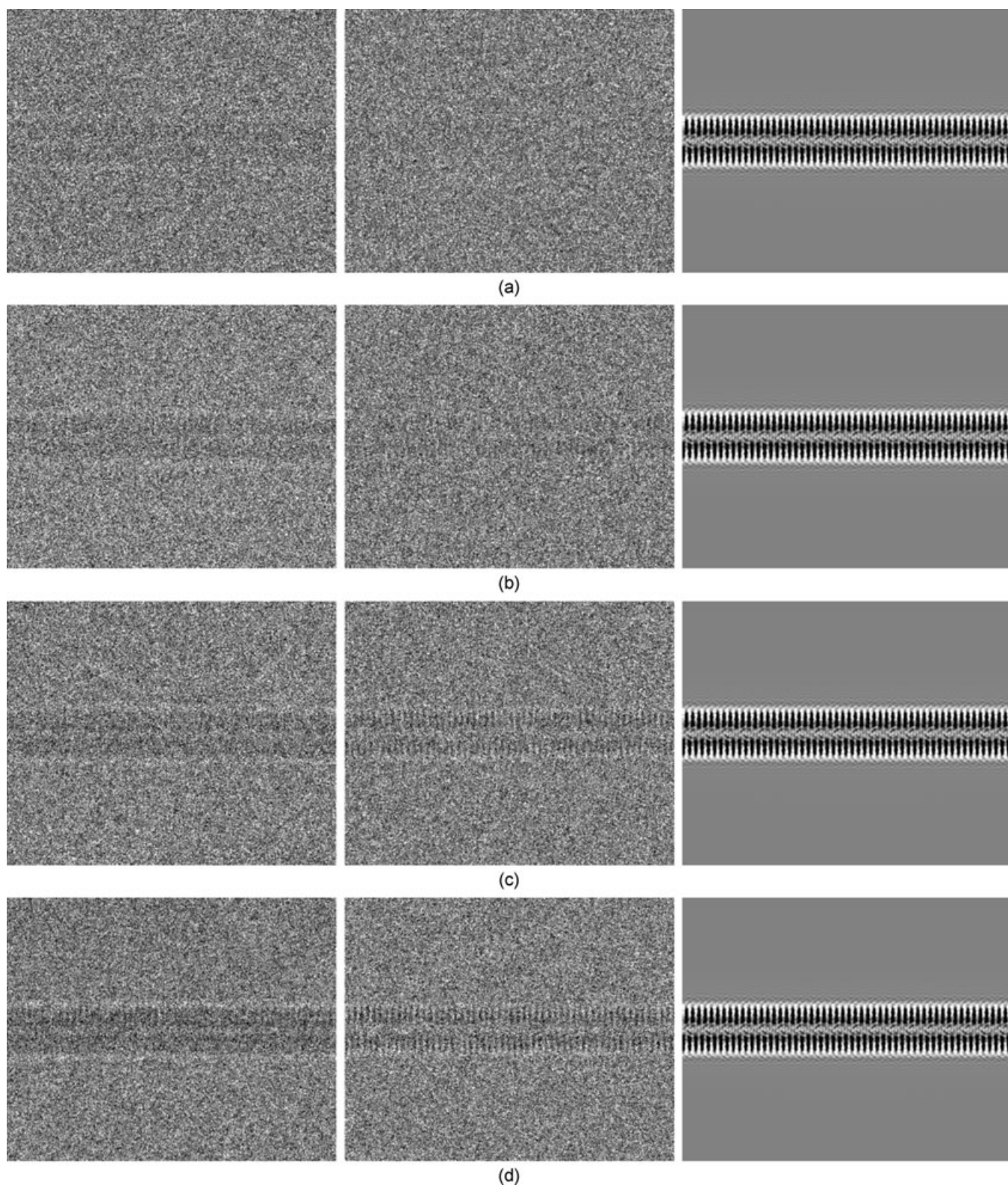


Fig. 6. TMV dose series: Each row shows experimental (left), simulated (middle), and noise-free simulated (right) images of a portion of a TMV virion acquired at a fixed dose using 66000 \times magnification and a nominal defocus of 3 μm . The dose values for the rows are as follows: 170 e^-/nm^2 (10 e^-/pixel , exposure time 0.2 s) in (a), 510 e^-/nm^2 (30 e^-/pixel , exposure time 0.5 s) in (b), 1700 e^-/nm^2 (100 e^-/pixel , exposure time 1.5 s) in (c), and 3500 e^-/nm^2 (210 e^-/pixel , exposure time 3.0 s) in (d). The corresponding intensity profiles are shown in Fig. 7.

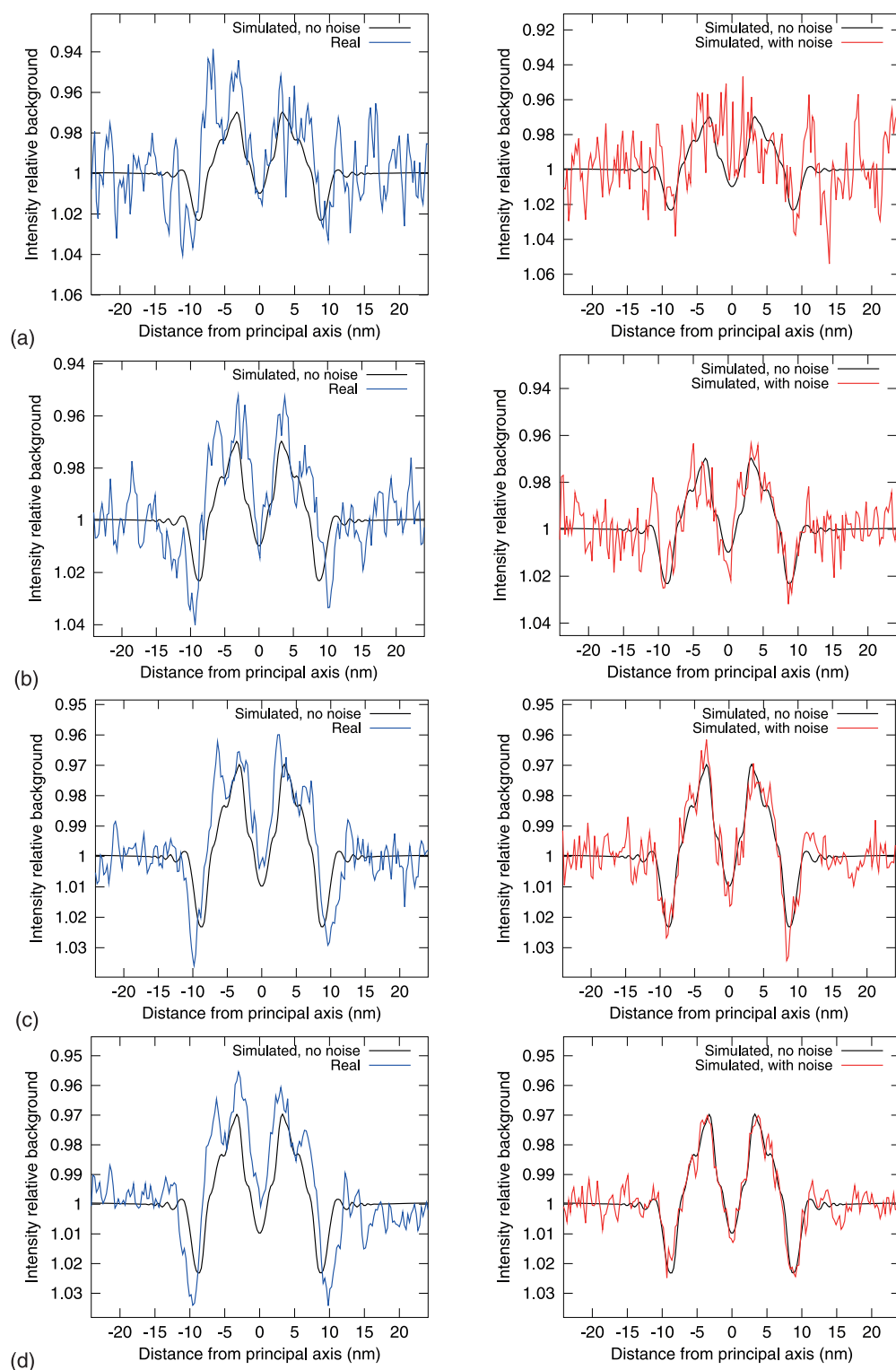


Fig. 7. Intensity profiles in a dose series: Each row compares intensity profiles of images of a TMV virion recorded using a fixed dose. The right figure compares profiles from noisy and noise-free simulated images and the left figure compares profiles from experimental and noise-free simulated images. The dose values used for the rows are as follows: The dose values for the rows are as follows: 173 e^-/nm^2 (10.26 e^-/pixel , exposure time 0.2 s) in (a), 510 e^-/nm^2 (30 e^-/pixel , exposure time 0.5 s) in (b), 1700 e^-/nm^2 (100 e^-/pixel , exposure time 1.5 s) in (c) and 3500 e^-/nm^2 (210 e^-/pixel , exposure time 3.0 s) in (d). The images are shown in Fig. 6.

exposure prevent a close analysis of the image. From 0.5 s and on the variance of the intensity is smaller and compatible with an analysis of the image of the virion; the two dense peaks, the less dense central channel and the surrounding bright rims can be discerned. It is obvious that when the dose increases the profile of the recorded image gets more and more similar to the predicted profile, and the two profiles are, in fact, quite similar after an exposure of 3.0 s. We conclude that the simulator can generate a series of TEM-like images that delineate the effects of electron dose on the phase contrast image of a molecular object in vitrified ice examined at underfocus. One final observation is that the uncertainty in the actual value of defocus used in experimental images implies that intensity profiles can only be used for validation when experimental and simulated images are acquired with a defocus that is high enough.

In conclusion, we have tested the ability of the simulator to generate proper TEM-like images by comparing simulated images of the TMV virion with experimental images obtained at different degrees of underfocus and with different electron doses. The simulated images with noise added closely resemble the experimental ones, indicating that the simulator should be a useful tool to evaluate TEM images and to properly plan TEM experiments (see also the discussion in Section 'Discussion').

Discussion

Our TEM simulator with associated phantom generator and calibration protocol offers a comprehensive framework for simulation of TEM images of biological *in vitro* specimens. The validation shows that we are able to accurately simulate TEM images of thin biological *in vitro* specimens that are weakly scattering. Simulation of thicker and/or strongly scattering specimens require a more refined model for the electron–specimen interaction. However, as the implementation is modular, there is room for introducing such improvements in the future.

Below we emphasize those aspects of our approach for simulation that we believe are unique along with a discussion of the validation procedure and the usefulness of our framework for simulation.

Unique aspects of our approach

Transparency. An important, and perhaps unique, aspect of our approach is transparency in the sense that we have gone to great lengths at deriving *all* models used by the TEM simulator and associated phantom generator from first principles within physics. This is also reflected in the implementation where the software components are clearly related to specific physics phenomena relevant for TEM imaging. Such a clear connection to the underlying physics is required if one seeks to have a software that is expandable. As an example, improved models for the electron–specimen interaction or models better suited for modelling new or different type of TEM instrumentation are easily incorporated into the simulation

without modifying the entire model for the image formation. A prime example of the latter would be to incorporate simulation of the new generation of fast direct electron detectors that have quite different noise characteristics when compared with traditional phosphor/fibre optics-coupled CCDs as discussed by Moldovan *et al.* (2008).

Phantom generator. Another important aspect of our simulator is related to the model for the absorption potential, and to some extent also the electrostatic potential, used by the phantom generator. These are generated using physical principles from an atomic model and they are given in volts. In many popular software packages, such as EMAN, the phantom created will be a map of electron density, rather than electrostatic potential that is needed for accurate TEM image simulation.

Another commonly used approximation is to assume that the absorption potential (the imaginary part of the potential) is a constant (the amplitude contrast ratio) times the electrostatic potential. We do not assume such a relation between the absorption and electrostatic potentials, instead both are independently generated using the PDB file.

Finally, in our case the potential for the solvent is generated using the same principles as for the molecules by means of an averaging procedure. There is also an option of adding a granularity. In other software packages for TEM simulation it is unclear what physics models are used for generating the potential for the solvent.

Noise. In our treatment, the various sources of noise have a clear relation to the physical imaging process and they are intertwined in a consistent manner to model the noise of the entire imaging process. Most TEM simulators simply model noise as additive Gaussian noise. In Xmipp one has the option of adding coloured noise in order to mimic the background granularity. Still, these noise models are all purely phenomenological without any connection to the physical sources of noise. Noise in our simulations is derived from a physics model for the Poisson process of electrons striking the detector. Rather than from some phenomenological additive noise term, the 'colour' in our noise model stems naturally from the detector elements that introduce correlations between neighbouring pixels.

Parameters and calibration. All parameters, except for the ones occurring in (17) for the MTF, have a clear physics interpretation. We also provide a calibration protocol for determining the values of all nuisance parameters. This is also novel in the context of TEM simulation and is required if the simulator is to faithfully replicate experimental images.

Validation

We have chosen to base our validation on comparison against images of TMV. This choice was in a sense natural as TMV virions are structurally well characterized and their

appearance in TEM images is well known. Simulated as well as experimental electron images were generated under very different conditions (variation with defocus and dose) and compared visually at the various conditions studied. We concluded that the generated images were very similar to the corresponding experimental images. To carry out the comparisons in a more objective manner, we also determined intensity profiles across the TMV virions, which confirmed that the intensity variations measured were very similar in simulated and experimental images. Thus, as far as we can judge, the simulator with the associated phantom generator delivers simulated TEM images that closely resemble the ones recorded in the electron microscope.

A more ambitious agenda would be to aim for a fully quantitative validation, i.e. to quantitatively describe specific aspects in the simulated and experimental images, usually referred to as Figures Of Merit (FOMs). However, this approach has proven most difficult with unstained biological objects. First, TEM images of unstained biological specimens have very low contrast, and it is, therefore, difficult to get reliable determinations of the FOMs. Furthermore, to handle the large number of imaging parameters needed (dose, defocus, magnification, ...), a statistical evaluation of the FOMs requires a huge number of experimental and simulated images. Finally, the attempt to single out the best simulated image for comparison often results in large-scale multi-parameter optimization problems. Together, at least presently, these challenges make it a very difficult task to base a validation on FOMs in studies of unstained biological specimens. It could be added that also in the material sciences dealing with much better characterized specimens, validation of simulators is usually done only visually, see e.g. Kirkland *et al.* (2008), Kirkland (2010), even though there are attempts at using FOMs as in Mobus *et al.* (1998), Tang *et al.* (1993), Tang *et al.* (1994), Saxton (1997).

Usefulness and significance

A simulator can be used in studies of both isolated objects and objects still positioned within the cell. For example, a simulator can assist in the identification and characterization of molecular objects in electron images; simulated 2D images can be generated from the molecular phantom and compared to the electron micrographs obtained. In a more advanced analysis, a phantom generator can be used in the docking process where atomic models are fitted into structural maps obtained by means of 3DEM. A simulator can also be a valuable tool to test whether a proposed 3D model of a macromolecule, a macromolecular assembly or a molecular arrangement is in agreement with the features of an object observed in the electron micrographs. In addition, a simulator could help assessing whether an electron microscopic approach is at all a good choice to solve a specific molecular problem using the methods and instruments available.

It should be stressed that a simulator could also be a critical tool in the development of novel EM techniques and procedures. For example, it will be possible to easily and cost-effectively investigate the impact of new data collection techniques and improved instrumentation. In addition, simulation will be helpful in the development and evaluation of computational techniques, both for 3D reconstruction as well as for 2D and 3D image processing techniques.

Concluding summary

The validation shows that the TEM simulator with associated phantom generator and calibration protocol is able to generate realistic TEM images of both aqueous buffer as well as TMV virions embedded in such buffer. As no parts of the simulation suite is specifically adapted to TMV, the same conclusion is also expected to hold for other thin unstained weakly scattering biological specimens. In total, we have a validated framework for accurate simulation of TEM imaging of such specimens. As the underlying methodology is described in detail, the approach used for simulation is transparent. Furthermore, the software and associated data are freely available from <http://tem-simulator.sourceforge.net> (see also <http://www.cmb.ki.se/research/cet>). The reference manual for the software also contains detailed and up-to-date installation instructions under various operating systems. Finally, the software suite has a modular implementation reflecting the logic dictated by the physics and mathematics. This makes it much easier to incorporate improvements into both the TEM simulator as well as the phantom generator.

Acknowledgments

We thank Hans Elmlund, Lars Norlén, Sara Sandin, Hans Hebert and Philip Koeck for valuable comments on the manuscript. Sidec is acknowledged for support in an early phase of the study. The research has been supported by the Swedish Research Council, the European Community (3D-EM Network of Excellence), the Carl Trygger Foundation and the Magnus Bergvall Foundation. The Knut and Alice Wallenberg Foundation is acknowledged for support to the electron microscope facility at the Department of Cell and Molecular Biology, Karolinska Institute.

References

- Al-Amoudi, A., Chang, J.-J., Leforestier, A., *et al.* (2004) Cryo-electron microscopy of vitreous sections. *EMBO J.* **23**, 3583–3588.
- Bajaj, C. & Goswami, S. (2006) Automatic fold and structural motif elucidation from 3D EM maps of macromolecules. *Proceedings of the International Conference Vision Graphics Image Processing, ICVGIP*, pp. 264–275.
- Baker, N.A., Sept, D., Joseph, S., Holst, M.J. & McCammon, J.A. (2001) Electrostatics of nanosystems: application to microtubules and the ribosome. *Proc. Natl. Acad. Sci. U.S.A.* **98**, 10037–10041.

- Chen, L., Holst, M.J. & Xu, J. (2007) The finite element approximation of the nonlinear Poisson–Boltzmann equation. *SIAM J. Numer. Anal.* **45**(6), 2298–2320.
- Clare, D.K. & Orlova, E.V. (2010) 4.6 Å Cryo-EM reconstruction of tobacco mosaic virus from images recorded at 300 keV on a 4k×4k CCD camera. *J. Struct. Biol.* **171**, 303–308.
- Dinges, C. & Rose, H. (1995) Simulation of filtered and unfiltered TEM images and diffraction patterns. *Phys. Stat. Solid. A. Appl. Mater. Sci.* **150**(1), 23–29.
- Dolinsky, T.J., Czodrowski, P., Li, H., Nielsen, J.E., Jensen, J.H., Klebe, G. & Baker, N.A. (2007) PDB2PQR: expanding and upgrading automated preparation of biomolecular structures for molecular simulations. *Nucl. Acids Res.* **35**, W522–525.
- Doyle, P.A. & Turner, P.S. (1968) Relativistic Hartree–Fock X-ray and electron scattering factors. *Acta Crystallogr. Sect. A* **24**(3), 390–397.
- Fanelli, D. & Öktem, O. (2008) Electron tomography: a short overview with an emphasis on the absorption potential model for the forward problem. *Inverse Problems* **24**(1), 013001.
- Frank, J. (2009) Single-particle reconstruction of biological macromolecules in electron microscopy – 30 years. *Quart. Rev. Biophys.* **42**, 139–158.
- Frank, J. & Shimkin, B. (1978) A new image processing software for structural analysis and contrast enhancement. *Electron Microscopy 1978; Papers Presented at the Ninth International Congress on Electron Microscopy, Toronto, Microscopical Society of Canada, Toronto, 1978* (ed. by J. M. Sturgess), vol. 1, pp. 210–211.
- Glaeser, R.M., Downing, K.H., DeRosier, D., Chu, W. & Frank, J. (2006) *Electron Crystallography of Biological Macromolecules*. Oxford University Press, Oxford.
- Glauber, R.J. (1959) High-energy collision theory. *Lectures in theoretical physics, Volume I. Lectures delivered at the Summer Institute for Theoretical Physics, University of Colorado, Boulder, 1958* (ed. by W. E. Brittin & L. G. Dunham), pp. 315–414. Interscience Publishers, New York–London.
- Gómez-Rodríguez, A., Beltrán-del Río, L.M. & Herrera-Becerra, R. (2009) SimulaTEM: multislice simulations for general objects. *Ultramicroscopy* **110**(2), 95–104.
- Hawkes, P.W. & Kasper, E. (1994) *Principles of Electron Optics*, vol. 3: Wave Optics. Academic Press, San Diego.
- Henderson, R. (2004). Realizing the potential of electron cryo-microscopy. *Quart. Rev. Biophys.* **37**, 3–13.
- Ishizuka, K. (1980) Contrast transfer of crystal images in TEM. *Ultramicroscopy* **5**, 55–65.
- Kirkland, A.I., Chang, L.-Y.S. & Hutchison, J.L. (2008) Atomic resolution transmission electron microscopy. *Science of Microscopy* (ed. by P. W. Hawkes and J. C. H. Spence), chapter 1, pp. 3–64. Springer Verlag, New York.
- Kirkland, E.J. (2010) *Advanced Computing in Electron Microscopy*. 2nd edn. Springer Verlag, New York.
- Leis, A., Rockel, B., Andrees, L. & Baumeister, W. (2009) Visualizing cells at the nanoscale. *Trends Biochem. Sci.* **34**(2), 60–70.
- Lucic, V., Forster, F. & Baumeister, W. (2005) Structural studies by electron tomography: from cells to molecules. *Ann. Rev. Biochem.* **74**, 833–865.
- Marabini, R., Rietzel, E., Schröder, R., Herman, G.T. & Carazo, J.-M. (1997) Three-dimensional reconstruction from reduced sets of very noisy images acquired following a single-axis tilt scheme: application of a new three-dimensional reconstruction algorithm and objective comparison with weighted backprojection. *J. Struct. Biol.* **120**, 363–371.
- Marabini, R., Herman, G.T. & Carazo, J.-M. (1998) 3D reconstruction in electron microscopy using ART with smooth spherically symmetric volume elements (blobs). *Ultramicroscopy* **72**, 53–65.
- McIntosh, R., Nicastro, D. & Mastronarde, D. (2005) New views of cells in 3D: an introduction to electron tomography. *Trends Cell Biol.* **15**, 43–51.
- Mobus, G., Schweinfest, R., Gemming, T., Wagner, T. & Rühle, M. (1998) Iterative structure retrieval techniques in HREM: a comparative study and a modular program package. *J. Microsc.* **190**(1), 109–130.
- Moldovan, G., Li, X., Wilshaw, P. & Kirkland, A.I. (2008) Direct electron detectors for TEM. In M. Luysberg, K. Tillmann, and T. Weirich, editors, *EMC 2008 14th European Microscopy Congress 1–5 September 2008, Aachen, Germany*. vol. 1: Instrumentation and Methods, pp. 85–86. Springer, New York.
- Müller, H., Rose, H. & Schorsch, P. (1998) A coherence function approach to image simulation. *J. Microsc.* **190**(1–2), 73–88.
- Namba, K. & Stubbs, G. (1986) Structure of tobacco mosaic virus at 3.6 Å resolution: implications for assembly. *Science* **231**, 1401–1406.
- Nickell, S., Förster, F., Linaudis, A., Del Net, W., Beck, F., Hegerl, R., Baumeister, W. & Plitzko, J.M. (2005) TOM software toolbox: acquisition and analysis for electron tomography. *J. Struct. Biol.* **149**(3), 227–234.
- Peng, L.M. (2005) Electron atomic scattering factors, Debye–Waller factors and the optical potential for high-energy electron diffraction. *J. Electr. Microsc.* **54**(3), 199–207.
- Peng, L.-M., Ren, G., Dudarev, S.L. & Whelan, M.J. (1996) Robust parameterization of elastic and absorptive electron atomic scattering factors. *Acta Crystallogr. Sect. A* **52**(2), 257–276.
- Reimer, L. & Kohl, H. (2008) *Transmission Electron Microscopy*. vol. 36: *Springer Series in Optical Sciences*, 5th edn. Springer Verlag, New York.
- Robinson, C.V., Sali, A. & Baumeister, W. (2007) The molecular sociology of the cell. *Nature* **450**, 973–982.
- Rose, H. & Müller, H. (2003) Electron scattering. *High-Resolution Imaging and Spectrometry of Materials* (ed. by F. Ernst and M. Rühle), Springer Series in Materials Science, chapter 2, pp. 9–66. Springer Verlag, New York.
- Saxton, O. (1997) Quantitative comparison of images and transforms. *J. Microsc.* **190**, 52–60.
- Shaikh, T.R., Gao, H., Baxter, W.T., Asturias, F.J., Boisset, N., Leith, A. & Frank, J. (2008) SPIDER image processing for single-particle reconstruction of biological macromolecules from electron micrographs. *Nat. Protocols* **3**, 1941–1974.
- Sorzano, C.O.S., Marabini, R., Boisset, N., Rietzel, E., Schröder, R., Herman, G.T. & Carazo, J.-M. (2001) The effect of overabundant projection directions on 3D reconstruction algorithms for electron microscopy. *J. Struct. Biol.* **133**(2–3), 108–118.
- Sorzano, C.O.S., Marabini, R., Velázquez-Muriel, J., Bilbao-Castro, J.R., Scheres, S.H.W., Carazo, J.M. & Pascual-Montano, A. (2004) XMIPP: a new generation of an open-source image processing package for electron microscopy. *J. Struct. Biol.* **148**(2), 194–204.
- Steven, A.C. & Baumeister, W. (2008) The future is hybrid. *J. Struct. Biol.* **163**, 186–195.
- Tang, D., Kirkland, A. & Jefferson, D. (1993) Optimisation of high-resolution image simulations: I. Image selection in real space. *Ultramicroscopy* **48**(3), 321–331.
- Tang, D., Kirkland, A. & Jefferson, D. (1994) Optimisation of high-resolution image simulations: II. Image selection in reciprocal space. *Ultramicroscopy* **53**(2), 137–146.

- Tang, G., Peng, L., Baldwin, P.R., Mann, D.S., Jiang, W., Rees, I. & Ludtke, S.J. (2007) EMAN2: An extensible image processing suite for electron microscopy. *J. Struct. Biol.* **157**(1), 38–46.
- Wall, J.S. (2006) Simulation of Coherent Scattering in the STEM. *Microsc. Microanal.* **12**(Supp 2), 1350–1351.
- Zhang, X., Bajaj, C., Kwon, B., Dolinsky, T.J., Nielsen, J.E. & Baker, N.A. (2006) Application of new multiresolution methods for the comparison of biomolecular electrostatic properties in the absence of structural similarity. *Multiscale Model. Simulat.* **5**(4), 1196–1213.
- Zuo, J.M. (2000) Electron detection characteristics of a slow-scan CCD camera, imaging plates and film, and electron image restoration. *Microsc. Res. Tech.* **49**(3), 245–268.

Appendix A: Definition and calculation of intensity profiles

An intensity profile is used for assessing the ability of the simulator to replicate the contrast variations exhibited in experimental images. The definition of the intensity profile needs to be adapted to the type of the objects contained in the reference specimen. In our case, the reference specimen is TMV virions in aqueous buffer, so the object is rod-like in appearance. Hence, the intensity profile we make use of is adapted to an object that is symmetrically repeating itself along a principal axis. Its precise definition is given as follows (cf. Fig. 1):

1. Specify a region of interest which is a sub-region of the TEM image (experimental or simulated) containing a portion of the object that is reasonably straight, and in case of experimental images, that does not have any ice crystals in its immediate vicinity (cf. Fig. 1a).
2. Extract the principal axis of the object within the region of interest (cf. Fig. 1a).
3. Project the region of interest along the principal axis thereby generating a 1D intensity profile (cf. Fig. 1b).

Appendix B: Calculation of scattering potentials

Here we provide precise details on how scattering potentials are calculated. As mentioned before, an approximation we make is that an object is regarded as a collection of isolated atoms, so it is natural to start out by considering the scattering potential of a free atom. Next, we consider how to deal with situations where we lack an atomic model. This leads us to constructing scattering potentials by an averaging.

The case of a free atom

The scattering potential models the electron–specimen interaction that is made visible by means of contrast variations in a TEM image. There are two underlying mechanisms that give rise to contrast variations, *amplitude (scattering)* and *phase (interference)* phenomena, and the corresponding contrast is referred to as *amplitude* and *phase contrast*. The former is contrast produced by the loss of amplitude from the beam

due to removal of electrons as they fall out-side the objective aperture. Phase contrast on the other hand originates from shifts in the relative phases of the portions of the beam which contribute to the image.

Both elastic and inelastic scattering contributes to phase and amplitude contrast. However, we currently do not have a good model for the contribution of inelastic scattering to phase contrast.

Phase contrast. The phase contrast is modelled by the real part of the scattering potential F , i.e. the electrostatic potential V .

Elastic scattering. A free atom with atomic number Z consists of a positively charged nucleus surrounded by a negatively charged electron cloud. The electric charges give rise to an electrostatic potential $V(\mathbf{x})$ at a point \mathbf{x} in space. Its 3D Fourier transform is called the (electron) scattering factor of the atom, i.e. the scattering factor is defined as the function

$$f_Z^{(e)}(\xi) := \frac{m_0 e}{2\pi \hbar^2} \int_{\mathbb{R}^3} V(\mathbf{x}) \exp(-4\pi i \xi \cdot \mathbf{x}) d\mathbf{x}, \quad (\text{B.1})$$

where m_0 is the electron rest mass, e is the elementary charge, and \hbar is the reduced Planck constant. An application of the Fourier inversion formula enables us to express the electrostatic potential in terms of the scattering factor

$$V(\mathbf{x}) = \frac{16\pi \hbar^2}{m_0 e} \int_{\mathbb{R}^3} f_Z^{(e)}(\xi) \exp(4\pi i \xi \cdot \mathbf{x}) d\xi. \quad (\text{B.2})$$

If the atom is spherically symmetric, the potential and the scattering factor are radial and can be written as functions of the radial variation only as argued for in Peng *et al.* (1996), Peng (2005) and Doyle & Turner (1968).¹ For the purpose of tabulating and performing calculations on scattering factors of different elements, a common parametrization is of the form

$$f_Z^{(e)}(\xi) = \sum_{i=1}^n a_i \exp(-b_i |\xi|^2), \quad (\text{B.3})$$

where the parameters a_i and b_i are chosen to give the best fit of the function in a chosen interval. Tabulated values of the parameters with $n = 4$ for most of the elements is given in Doyle & Turner (1968) and Peng *et al.* (1996) gives values with $n = 5$ for all the stable elements. Substituting (B3) into (B2) gives the following expression for the electrostatic potential

$$V(\mathbf{x}) = \frac{16\pi^{5/2} \hbar^2}{m_0 e} \sum_{i=1}^n \frac{a_i}{b_i^{3/2}} \exp\left(-\frac{4\pi^2 |\mathbf{x}|^2}{b_i}\right). \quad (\text{B.4})$$

The tabulated parameter values are conventionally given in Åunits, therefore $|\mathbf{x}|$ should also be measured in Å when used in this formula. The numerical value for the scaling factor preceding the sum in (B4) is

$$\frac{16\pi^{5/2} \hbar^2}{m_0 e} = 2132.79 \text{ Å}^2 \text{V} \quad (\text{B.5})$$

¹ Note however that in Peng *et al.* (1996) and Peng (2005) the potential refers to the potential energy of an electron, which differs from V by a factor e . Also, in Peng *et al.* (1996, eq. 2) (which corresponds to (B2) above) is wrong by a factor $16\pi^2$.

so if $|\mathbf{x}|$ is measured in Å and the parameters a_i and b_i are taken from tables, the potential measured in V is given by

$$V(\mathbf{x}) = 2132.79 \cdot \sum_{i=1}^n \frac{a_i}{b_i^{3/2}} \exp\left(-\frac{4\pi^2|\mathbf{x}|^2}{b_i}\right). \quad (\text{B.6})$$

These formulae can easily be modified to yield a low pass filtered version of the potential. Suppose we want to compute the potential low pass filtered to resolution R . This means that spatial frequencies above $1/(2R)$ should be close to 0. This can be accomplished by multiplying the scattering factor in (B3) by $\exp(-(4R|\boldsymbol{\xi}|)^2)$, since the spatial frequency corresponds to $2|\boldsymbol{\xi}|$. This means that a potential at resolution R will be obtained by adding the quantity $16/R^2$ to each b_i before using the formula (B4).

The presence of a Debye–Waller factor B , which accounts for thermal vibrations of an atom, might also be included in the model by adding B to each parameter b_i . This amounts to a blurring of the atom, which models its average potential. However, each individual electron passing through the sample sees the atoms essentially in a fixed position, not the long-time average of the potential, and properly modelling the effects of thermal vibrations is likely to be more complicated than just blurring the potential of each atom.

Amplitude contrast. The amplitude contrast is modelled by the imaginary part of the scattering potential F , i.e. V_{abs} . The latter is derived from the (elastic and inelastic) cross sections as shown below. It is worth pointing out that while the real part of the potential only depends on the atoms in the sample, the imaginary part also depends on electron energy and the opening of the aperture.

Cross sections and the absorption potential. First, the interpretation of cross section is as follows: Consider a solid angle Ω . An area σ perpendicular to the direction of the beam, such that electrons passing through this area get (elastically or inelastically) scattered into the solid angle Ω is known as a (elastic or inelastic) cross section for scattering into Ω . If the solid angle Ω is made infinitesimally small, the ratio $d\sigma/d\Omega$ is known as the differential cross section. Hence, the cross section for scattering to angles higher than some threshold α is then obtained by integrating the differential cross section:

$$\sigma(\alpha) = \int_{\theta \geq \alpha} \frac{d\sigma}{d\Omega} 2\pi \sin \theta d\theta. \quad (\text{B.7})$$

Now, we would like to add an imaginary part $V_{\text{abs}}(\mathbf{x})$ to the real part $V(\mathbf{x})$ of the potential F in order to absorb the electrons which are in reality scattered outside the aperture. For simplicity, we assume the absorption potential of a single atom to be of the form

$$V_{\text{abs}}(\mathbf{x}) = a \exp(-b|\mathbf{x}|^2) \quad (\text{B.8})$$

and the problem is now to relate a and b to the scattering cross sections.

Suppose first that the phantom contains a region of thickness h and area A in which the potential is iV_0 . The electron wave passing through this region will be damped by a factor

$$\exp\left(-\frac{1}{2k} \frac{2me}{\hbar^2} V_0 h\right). \quad (\text{B.9})$$

The intensity is proportional to the square of the amplitude, in other words it is damped by a factor

$$\exp\left(-\frac{2me}{k\hbar^2} V_0 h\right) \approx 1 - \frac{2me}{k\hbar^2} V_0 h. \quad (\text{B.10})$$

This corresponds to a scattering cross section of

$$\sigma = \frac{2me}{k\hbar^2} V_0 h A = \frac{2me}{k\hbar^2} \int_{\mathbb{R}^3} V_{\text{abs}}(\mathbf{x}) d\mathbf{x}. \quad (\text{B.11})$$

If the same relation is applied when V_{abs} is of the form (B8), we find that

$$\sigma = \frac{2me}{k\hbar^2} \int_{\mathbb{R}^3} V_{\text{abs}}(\mathbf{x}) d\mathbf{x} = \frac{2me}{k\hbar^2} a \left(\frac{\pi}{b}\right)^{3/2}. \quad (\text{B.12})$$

By setting this equal to the sum of elastic and inelastic cross sections the following formula is obtained for a

$$\begin{aligned} a &= \frac{k\hbar^2}{2me} \left(\frac{b}{\pi}\right)^{3/2} (\sigma_{\text{el}}(Z, \alpha) + \sigma_{\text{inel}}(Z, \alpha)) \\ &= \frac{\hbar^2}{2m_0 e} \frac{kE_0}{E + E_0} \left(\frac{b}{\pi}\right)^{3/2} (\sigma_{\text{el}}(Z, \alpha) + \sigma_{\text{inel}}(Z, \alpha)). \end{aligned} \quad (\text{B.13})$$

The value of b can be chosen arbitrarily, keeping in mind the grid on which the function will be sampled.

Elastic scattering. In the Born approximation, the differential cross section for elastic scattering to angle θ is related to the scattering factor by

$$\frac{d\sigma_{\text{el}}}{d\Omega} = \left| \frac{m}{m_0} f_Z^{(\text{e})}(\boldsymbol{\xi}) \right|^2, \quad (\text{B.14})$$

where m is the relativistic mass of the electron,

$$|\boldsymbol{\xi}| = \frac{k \sin(\theta/2)}{2\pi} \approx \frac{k\theta}{4\pi} \quad (\text{B.15})$$

and k is the wave number of the electron wave, so

$$k = \frac{1}{\hbar c} \sqrt{E(E + 2E_0)} = \frac{e}{\hbar c} \sqrt{U_{\text{acc}}(U_{\text{acc}} + 2U_0)}. \quad (\text{B.16})$$

Here the scattering angle θ is defined as the angle between the scattered and the unscattered beam.²

For large scattering angles, an approximation of the form

$$f_Z^{(\text{e})}(\boldsymbol{\xi}) = \frac{m_0 e^2 Z}{8\pi \hbar^2 \epsilon_0 (|\boldsymbol{\xi}|^2 + s_0^2)} \quad (\text{B.17})$$

² It should be noted that some references define the scattering angle as half of the angle between the scattered and unscattered beam, and the formulae will then be changed accordingly.

is sometimes used, where h is the Planck constant, ε_0 the permittivity of vacuum, and s_0 is a constant depending on the atomic number Z , e.g. Reimer & Kohl (2008) uses a formulae which amounts to taking

$$s_0 := \frac{Z^{1/3} m_0 e^2}{4 \varepsilon_0 h^2} = \frac{Z^{1/3}}{4 \pi a_H} \quad (\text{B.18})$$

with a_H denoting the Bohr radius for the Hydrogen atom.

Inelastic scattering. In Reimer & Kohl (2008, eq. (6.4)), an approximate formula for the inelastic cross section is given. According to this formula, the inelastic cross section of an atom for scattering to angles bigger than α is given by

$$\sigma_{\text{inel}}(Z, \alpha) = 4\pi Z \left(\frac{E + E_0}{k E_0} \right)^2 \cdot \left(\frac{2}{Z^{2/3}} \ln \left(1 + \frac{Z^{2/3}}{a_H^2 k^2 \alpha^2} \right) - \frac{1}{Z^{2/3} + a_H^2 k^2 \alpha^2} \right). \quad (\text{B.19})$$

This formula is not valid for very small scattering angles $\alpha \ll 1$ mrad, but the angles relevant in TEM are approximately 10 mrad, so for our purposes there should be no problem.

Average electrostatic potential

For the electrostatic potential, the volumetric integral of the potential is given by

$$\int_{\mathbb{R}^3} V(\mathbf{x}) d\mathbf{x} = \frac{2\pi \hbar^2}{m_0 e} f_Z^{(e)}(\mathbf{0}) = 47.8776 \cdot \sum_{i=1}^n a_i \quad (\text{B.20})$$

measured in $\text{\AA}^3 \text{V}$. This is useful for computing the average background potential of the solvent. If the solvent contains N molecules per unit volume, and each molecule contains n_Z atoms of type Z , then the average background potential V^{sol} is given by

$$V^{\text{sol}} = \frac{2\pi \hbar^2}{m_0 e} N \sum_Z n_Z f_Z^{(e)}(\mathbf{0}). \quad (\text{B.21})$$

Applying this to water gives the background potential

$$V_{\text{water}} = 47.8776 \cdot 0.0335 \cdot (f_{Z=8}^{(e)}(\mathbf{0}) + 2 f_{Z=1}^{(e)}(\mathbf{0})) \approx 4.871 \text{ V}. \quad (\text{B.22})$$

Finally, the absorption potential of the surrounding solvent can be computed as

$$V_{\text{abs}}^{\text{sol}} = \frac{\hbar^2}{2m_0 e} \frac{k E_0}{E + E_0} N \sum_Z n_Z (\sigma_{\text{el}}(Z, \alpha) + \sigma_{\text{inel}}(Z, \alpha)), \quad (\text{B.23})$$

where N and n_Z have the same meaning as in (B.21) and

$$\frac{\hbar^2}{2m_0 e} = 3.80998 \text{ \AA}^2 \text{V}. \quad (\text{B.24})$$